SUBCRITICAL CRACK GROWTH INDUCED BY STRESS CORROSION IN QUASIBRITTLE MATERIALS

by

Weijin Wang

Bachelor of Engineering, Southwest Jiaotong University, 2011

Master of Science, University of Pittsburgh, 2013

Submitted to the Graduate Faculty of

Swanson School of Engineering in partial fulfillment

of the requirements for the degree of

Doctor of Philosophy

University of Pittsburgh

2017

UNIVERSITY OF PITTSBURGH

SWANSON SCHOOL OF ENGINEERING

This dissertation was presented

by

Weijin Wang

It was defended on

November 29th, 2016

and approved by

Qiang Yu, Ph.D., Assistant Professor, Department of Civil and Environmental Engineering

Albert To, Ph.D., Associate Professor, Department of Mechanical Engineering and Materials Science

Jeen-Shang Lin, Sc.D., Associate Professor, Department of Civil and Environmental Engineering

John Brigham, Ph.D., Senior Lecturer, School of Engineering and Computing Sciences at Durham University

Dissertation Director: Qiang Yu, Ph.D., Assistant Professor, Department of Civil and Environmental Engineering

SUBCRITICAL CRACK GROWTH INDUCED BY STRESS CORROSION IN QUASIBRITTLE MATERIALS

Weijin Wang, PhD

University of Pittsburgh, 2017

For concrete structures, a primary driver of deterioration shortening their lifespans is the damage growth resulting from coupled chemo-mechanical attack. Under sustained service load coupled with corrosion, stress corrosion cracking will happen and lead to subcritical crack growth (SCG) in concrete members. Thus, knowledge of the SCG in cement-based materials subject to concurrent physical and chemical attacks is of great importance for understanding and mitigating the chemo-mechanical deterioration in concrete structural members.

In this thesis, the SCG in hardened cement pastes is investigated experimentally by a novel test approach aided with micro-characterization. Specimens of negative geometry are designed, which enable the use of load control to trigger stable crack propagation in hardened cement pastes. Specimens from the same batch of mixture (with water/cement ratio w/b = 0.35 and 0.40) are exposed to the same chemical condition and loaded at the same age for both the static fatigue and stress corrosion groups. The average trend and the associated variation of the dependence of crack velocity v on the stress intensity factor K at the crack tip are obtained by using a high-resolution microscopy system to trace the crack tip. Three distinctive regions are captured in the K-v curves of stress corrosion specimens, which is different from those in static fatigue. With the help of advanced techniques including SEM, AFM and Raman spectroscopy, the microstructure destruction and chemical composition change induced by the imposed chemo-mechanical attack are characterized at different stages. In addition to the physical insights for

deeper understanding of the coupled effect of chemo-mechanical attack, these experimental results provide important macro- and microscopic benchmarks for numerical modeling.

Moreover, anchored at the obtained experimental benchmarks, material modeling and numerical schemes are developed to approximate the coupled chemo-mechanical deterioration in cement-based materials. To utilize the unique physical or chemical laws involved in each individual deterioration process, a two-dimensional (2D) discrete model consisting of two lattice systems is constructed in this study to approximate the meso-structure of cementitious materials. These two lattice systems, one approximating the dissolution of cement matrix under calcium leaching and the other simulating the response of material skeleton to external loads, are interlinked by a common physical variable – the porosity of hardened cement pastes, which evolves with the interaction of skeleton cracking and cement dissolution. To reduce the computational cost, an artificial time scale, which allows coarse temporal discretization, is used in the numerical framework resting on a hybrid of implicit and explicit formulation. The model is implemented in ABAQUS and validated by the experimental results. The numerical results show that the proposed discrete model can realistically describe the SCG in hardened cement pastes subject to coupled mechanical damage and calcium leaching.

TABLE OF CONTENTS

LIST OF TABLES

LIST OF FIGURES

ACKNOWLEDGEMENTS

First and foremost I would like to express my sincere appreciation to my Ph.D. advisor, Dr. Qiang Yu. Dr. Yu has offered me enormous assistance and guidance throughout my Ph.D. study, inspired me with innovative ideas, motivated me greatly with his enthusiasm in research and encouraged me to grow into an independent researcher. We started the research together with a novel idea, carried it out with a well-organized schedule and overcame the challenges and obstacles in this special journey. 'No pain no gain and never give up' is what I learned from him and my Ph.D. work. I appreciate all his contributions of time and advice to make my research substantial and stimulating.

I would also like to thank my committee members: Dr. Albert To, Dr. Jeen-Shang Lin and Dr. John Brigham, for their insightful instructions and supportive comments and suggestions. It is my great fortune to study here as their students. I thank them so much for their help and guidance, which strengthen my academic foundation and enrich my research experience. The members of our group have contributed immensely to my work and life at the University of Pittsburgh. I would like to thank my two colleagues, Chunlin Pan and Teng Tong, for their friendship as well as collaboration. We worked closely in different projects. I am especially thankful for their time and assistance in casting specimens as well as setting up the test device. I would also like to thank other group members: Hirut Kollech, Jie Zhang, Mingzhou Li, Renwick D'Souza, Sen Wang, Zhou Fan; and Dr. Qiong Liu. We together formed a diverse but united research team and created an enjoyable work environment.

Furthermore, I would like to thank our lab technician Charles Hager. Without his help, these specially-designed testing setups could have never been built. I also want to thank him for his patience and timely assistance in discussing and solving various experimental issues with me during my Ph.D. research.

My time in the University of Pittsburgh since 2011 has been stressful but also enjoyable. Many respectable professors and good friends I met here will become a part of my life. This wonderful experience would never come true without the supporting and trust of my dear parents, who have always been selflessly dedicated to supporting my education and life. Pursuing a Ph.D. degree is not only my dream, but also a dream of theirs which they haven't got a chance to achieve. My parents have been my role models ever since I was a little kid. This time, I hope they can feel proud of me.

Finally, I would like to express my special gratitude to my beloved fiancé, Wei Fu, for his accompany, encouragement, understanding and support. It has been 9 years since we first met in Southwest Jiaotong University. He overcame every obstacle, traveled 7,519 miles, joined me in the University of Pittsburgh to pursue a Ph.D. degree together with me. Without him and his love, this thesis would have never been completed.

To my beloved ones

1.0 INTRODUCTION

1.1 BACKGROUND

Concrete is one of the most popular construction materials all over the world. It mainly consists of fine and coarse aggregates bonded together by hardened cement paste. To ensure the safety and serviceability of structures, concrete is designed and expected to maintain its properties throughout its lifetime expectation, which is significantly prolonged with the increasing demands for construction sustainability. However, concrete will gradually degrade due to the deterioration processes induced by a wide range of environmental conditions as well as many physical factors, which include creep and shrinkage, carbonation, calcium leaching, acid attack, free-thaw damage, weathering process, to name a few. This property degradation substantially shortens the lifetime of concrete. Therefore, in order to predict and assess the structural performance, it is necessary to understand the deterioration processes in concrete.

The subcritical crack growth (SCG) in the micro- and meso-structures is one of the primary causes of degradation in many engineering materials including cementitious materials like concrete, mortar and cement paste. If the growth of a pre-existing crack is triggered by a sustained load, this phenomenon is conventionally described as SCG under static fatigue; while if the load is combined with chemical attacks, the occurrence of crack growth is considered as SCG under stress corrosion. Cement-based materials are susceptible to SCG due to the existence

of many subcritical cracks in their heterogeneous micro- and meso-structures. During service, concrete structures not only carry the service loads but also are exposed to the environment-induced hazards, many of which lead to chemical attacks weakening the microstructure of concrete.

A number of experiments (Wiederhorn, 1967; Freiman, Mulville and Mast, 1973; Wiederhorn *et al.*, 1982; Atkinson, 1984; Swanson, 1984) have reported accelerated strength loss and other property degradation due to the destruction of concrete microstructure when coupled chemo-mechanical attacks were applied. Dictated by the coupled chemo-mechanical deterioration, subcritical cracks will grow with time and finally develop into macro-cracks penetrating into concrete structures, even when the individual deterioration process alone is not critical for initiating crack propagation and coalescence. Therefore, to mitigate the risk of premature serviceability loss and ensure the safety of concrete structures, it is of great importance to understand the kinetics of SCG in cement-based materials subject to chemo-mechanical deterioration.

This study is aimed at making a comprehensive investigation of the SCG in hardened cement paste specimens under static fatigue and stress corrosion caused by calcium leaching. Plain cement paste is used to aid in isolating the coupled chemo-mechanical process from other influences triggered by the non-homogeneous interfaces between cement paste matrix and coarse aggregates in concrete. Furthermore, to accelerate the calcium leaching process, ammonium nitrate solution (NH_4NO_3) will be used.

1.1.1 Principle of Subcritical Crack Growth

Topics of SCG subject to stress corrosion are related to the concepts of corrosion growth and fracture mechanics. One of the critical parameters within fracture mechanics is the stress intensity factor *K* proposed in 1958 (Irwin, 1958). Generally, *K* is used to characterize the stress concentration at the crack tip. It measures the material capability to resist fracture and the stress state around the crack tip is considered as a function of crack configuration and remote load. In general, the stress state of an arbitrary crack can be described by one of the three fundamental fracture modes (Figure 1) or a mixed mode of them:

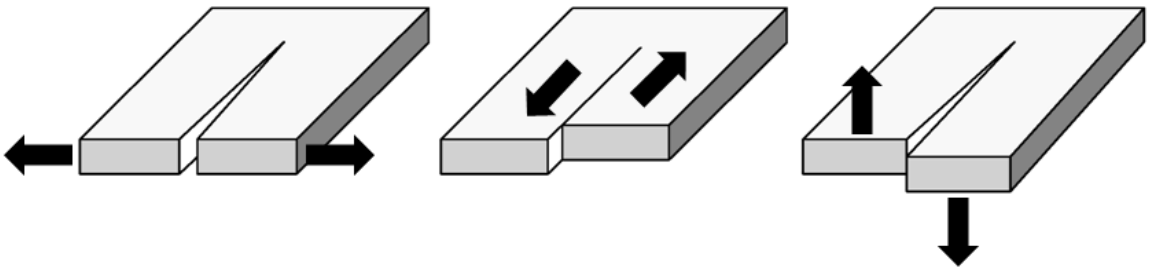

Figure 1. Three fracture modes

Mode I: Opening mode due to pure tensile stress;

Mode II: In-plan shear mode;

Mode III: Out-of-plane shear mode.

For Mode I fracture, the stress state around the crack tip can be expressed by the stress intensity factor (Lawn and Wilshaw, 1975) as:

$$\sigma_{ij} = \frac{K_I}{\sqrt{2\pi r}} \cdot f_{i,j}(\theta) \tag{1}$$

where σ_{ij} is the stress in Cartesian coordinate system (i, j), K_I is the stress intensity factor (K_I for mode I, K_{II} for mode II, K_{III} for mode III, respectively), r and θ are transformations of (i, j) in polar coordinate system, and $f_{i,j}(\theta)$ is a function of θ which depends on the specimen geometry. More conveniently, stress intensity factor for mode I fracture (K_I) can be written in terms of the strain energy release rate as:

$$\begin{aligned} K_I &= \sqrt{GE} && \text{For plane stress condition} \\ K_I &= \sqrt{\frac{GE}{(1-\nu^2)}} && \text{For plane strain condition} \end{aligned} \tag{2}$$

where G is the energy release rate, E is the Young's Modulus and ν is the Poisson's ratio.

1.1.2 *K-v* Trend and Test Methods for Subcritical Crack Growth

A crack can propagate either in a stable way or in an unstable way (Mai and Atkins, 1980). Under load control, stable crack propagation requires that a crack only grows when the applied load is increased. Unstable crack propagation develops in a spontaneous way and does not need additional load. In a brittle material, a sharp crack will immediately be initiated when the critical value of stress intensity factor (fracture toughness K_{IC}) is exceeded. However, previous studies have also shown that cracks developed when stress intensity factors were below K_{IC} (Wiederhorn, 1967, 1968; Atkinson, 1982). This is called SCG (Wiederhorn *et al.*, 1982; Swanson, 1984). The

velocity of SCG depends on the applied load as well as the material properties (Cai, 2012) and it is usually below 10^{-3} m/s for concrete, mortar and cement paste.

A number of experimental methods (Evans, 1972; Freiman, Mulville and Mast, 1973; Williams and Evans, 1973; Janssen, 1977) have been designed in the last several decades to characterize the kinetics of SCG in engineering materials, which is usually described by the dependence of crack velocity v on the stress intensity factor K at the crack tip. To obtain the K-v curves of engineering materials, there are three major experimental methods: 1) The double-torsion (DT) test (Evans, 1972; Williams and Evans, 1973); 2) The double-cantilever beam (DCB) test (Freiman, Mulville and Mast, 1973); and 3) The double-cleavage drilled-compression (DCDC) test (Janssen, 1977).

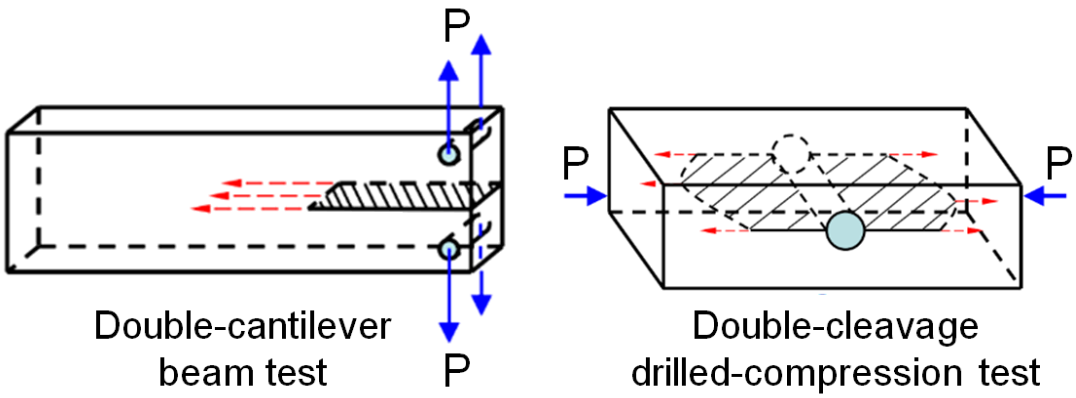

Figure 2. A typical set up of (left) DCB test and (right) DCDC test (Cai 2012)

The DCB test is mainly designed to obtain the fracture parameters such as K_{IC} for brittle materials (Freiman, Mulville and Mast, 1973). The specimen used in this test is a beam with one end being split into two cantilevers (Figure 2). Since the specimen is of positive geometry (K increases with crack length a) and K at the crack tip depends on the crack length, displacement control will be needed to keep stable crack propagation (Gonzalez and Pantano, 1990). The

DCDC test is mainly used to investigate fracture behavior of monolithic brittle materials such as glass or bi-materials (He, Turner and Evans, 1995). The specimen used in this test is a rectangular bar with a circular hole (Figure 2). Stable mid-plane crack growth can be achieved by axial compressive loading on the specimen. In this test, the crack propagation needs to be tracked.

Compared with the DCB and the DCDC tests, the DT test is the most widely used experimental method. It was initially developed for soda lime glass subject to static fatigue or stress corrosion (Evans, 1972). A typical setup of DT test is illustrated in Figure 3, where the double torsion induced by the applied load *P* leads to pure mode-I fracture at the notch tip (Evans, 1972; Williams and Evans, 1973; Shyam and Lara-Curzio, 2006). At the tip of the notch, a subcritical crack is expected to initiate and propagate along the centerline of the specimen. In order to make sure that the crack will propagate along the center line of the specimen, a guiding groove is generated on the top surface of the specimen.

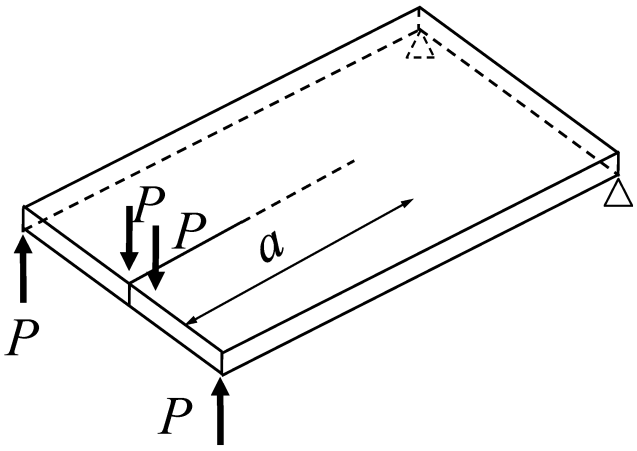

Figure 3. A typical setup of DT test

The theory of DT test originates from the empirical linear compliance relationship, which describes the load-displacement relationship of a DT specimen at the loading point (Shyam and Lara-Curzio, 2006). Plane stress condition is assumed due to the thin thickness of the specimen

and mode-I fracture at crack tip was verified by Evans and Williams's studies (Evans, 1972; Williams and Evans, 1973). By assuming that the shape of crack tip remains during crack propagation, the crack extension is expressed by the change rate of crack-surface-area (Fuller, 1979).

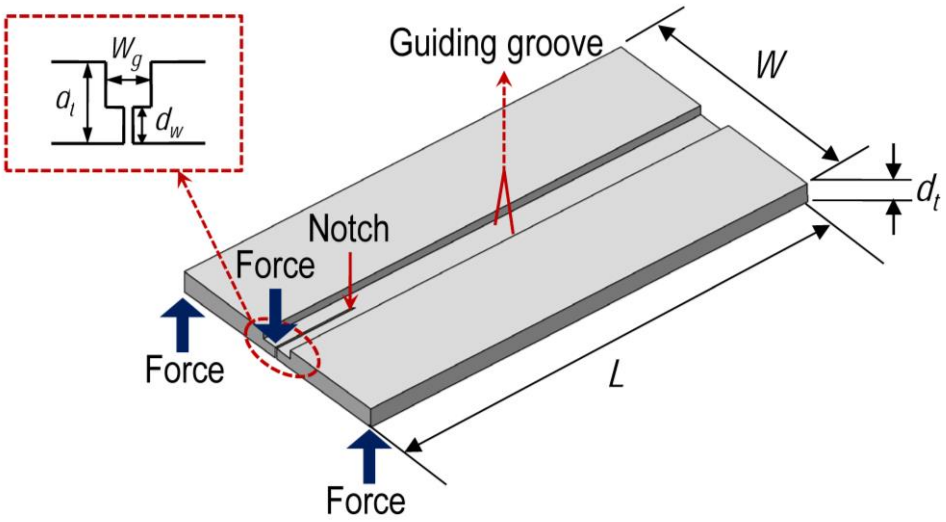

Figure 4. Illustration of the DT specimen used in Cai's study (Cai 2012)

Within the framework of linear elastic fracture mechanics (LEFM), the relationship between Young's modulus E and the stress intensity factor K_I can be connected through the elastic strain energy release rate G (Cai, 2012). Later, by introducing an analytical expression of the compliance λ and a correction function of specimen thickness $\varphi(z)$ (Williams and Evans, 1973), K_I for a DT specimen in Cai's study (Cai, 2012) is finally expressed as:

$$K_I = Pw_m \sqrt{\frac{3S(1+\nu)}{d_w d_t^3 SW\varphi(z)}} \tag{3}$$

where $\lambda = \left[\frac{3w_m^2}{SWd_t^3\varphi(z)}\right]a$; $\varphi(z) = 1 - 0.6302z + 1.20z\exp\left(-\frac{\pi}{z}\right)$; a is the crack length; w_m is the applied load moment arm; S is the shear modulus; d_w and d_t are the thickness of the crack front at the guiding groove and that of the whole specimen; W is the width of the rectangular plate; z is the thickness ratio as $z = \frac{2d_t}{W}$, respectively (See Figure 4). z and $\varphi(z)$ are dimensionless values. Similarly, with the benefit of the linear compliance λ (Williams and Evans, 1973), the crack velocity v at constant displacement at loading point can be expressed as (Cai, 2012):

$$v = -\frac{P_i a_i}{P^2}\left(\frac{dP}{dt}\right)_\Delta = -\frac{P_f a_f}{P^2}\left(\frac{dP}{dt}\right)_\Delta \tag{4}$$

Where *i* and *f* represent the corresponding values at initial and final stage, respectively.

According to Eq. 3 and 4, a salient property of DT test is that during the crack propagation along the guiding groove in the rectangular plate, the stress intensity factor K at crack tip is dependent on the load P, but independent of the crack length a (Evans, 1972). Thus, in order to attain a K-v curve, the displacement at the loading points must be controlled as a constant one in the DT test so as to relax the load P with crack propagation.

The DT test has been applied in a variety of engineering materials including metals, ceramics, glass and polymers (Wiederhorn, 1967, 1968; Nadeau, Mindess and Hay, 1974; Wecharatana and Shah, 1980; Atkinson, 1982, 1984; Beaudoin, 1985). The K-v curves obtained in these materials are schematically depicted in Figure 5. Typically, in the double-logarithmic scale, three distinctive regions, namely Regions I, II and III respectively, will sequentially appear during the course of crack growth in stress corrosion test; see Figure 5(a). It is very different

from the crack growth in static fatigue test, for which the *K*-*v* curve is almost a straight line in the double-logarithmic scale; see Figure 5(b).

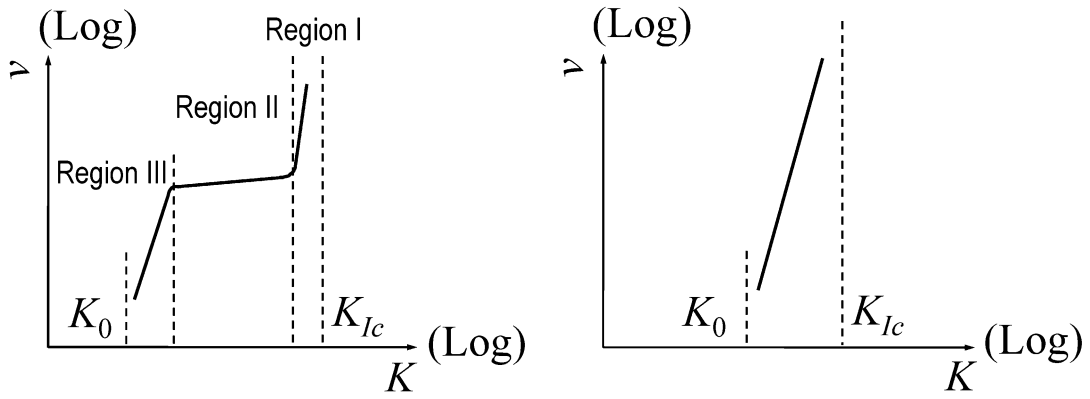

Figure 5. (a) Schematic illustration of a *K*-*v* curve under stress corrosion, (b) schematic illustration of a *K*-*v* curve under static fatigue

For SCG in stress corrosion, Region I is the first part developed in a *K*-*v* curve. The slope of the curve is steeper than those in the regions II and III. Rapid cracking occurs in this region but crack still propagates in a stable way. Within this stage, crack velocity *v* mainly depends on K_I and is mostly independent of environmental conditions. In other words, the mechanical behavior is dominant in this region (Wiederhorn *et al.*, 1982).

When the curve develops into Region II, the slope of the curve becomes mild. Crack velocity shows little change at different stress intensity factors (Freiman, 1984). When the curve travels to Region III, the slope turns steep again, but it won't be steeper than that in Region I. Crack evolution depends both on the material and the environmental conditions. In this stage, environmental-assist deterioration process around the crack tip dictates the crack development (Cai, 2012).

There is significant difference among the three regions in a *K*-*v* curve. The reason for it is that the rate of crack growth is governed by the transport of corrosive species in Region II and controlled by the chemical-enhanced fracture in Region III. Obviously, quantifying the kinetics of SCG in these three regions, especially in Regions II and III, is of essential importance to understand the effect of intertwined deterioration mechanisms in cement-based materials.

1.1.3 Discussions of DT test

As the most widely used method to study SCG in quasi-brittle cementitious materials, the DT test at constant displacement has significant advantages in obtaining stable crack propagation as well as a complete *K*-*v* curve in each single test. To export and record real-time force and displacement at loading-point of a DT specimen, a force cell and a linear-variable displacement transducer (LVDT) with considerable high accuracy are required. However, for a stress corrosion test under concurrent chemo-mechanical attacks, this method has significant limitations, which obstruct a comprehensive investigation of SCG in concrete and other cementitious materials.

First of all, a sophisticated equipment is needed to generate constant displacement at the loading point in a DT specimen. The loading point should be stationary during the test. The instantaneous force and final force are recorded by the force cell. Since the *K*-*v* diagram totally depends on the data obtained from experiment, high accuracy of measurements has to be guaranteed (e.g. ±2 μm for LVDT, ±0.1% for force cell from Cai 2012). However, in a stress corrosion test, corrosive solutions are used and the DT specimen, as well as parts of the loading equipment, will be immersed into the liquid. Thus, chemical species will corrode the equipment or even damage it.

Another challenge that restricts the application of DT tests to stress corrosion test is the high cost. One DT setup can test only one specimen at a single time. Thus, it is very hard to test a number of specimens from one same batch of concrete (or mortar and cement paste) simultaneously, which is actually essential for us to obtain the statistic information of SCG. Due to the unique challenges stemming from the nature of cement-based materials, unlike glass and ceramics, they have highly heterogeneous micro- and meso-structures, exhibit substantial material randomness, and are very age-sensitive. Therefore, to quantify the kinetics of SCG in stress corrosion and assess the associated scatter during the coupled deterioration processes, multiple specimens, cast from the same batch of mixture and exposed to the same chemical conditions, must be tested at the same age. To meet this requirement, multiple sets of sophisticated testing systems consisting of load cells and frames, displacement transducers, controllers, and data acquisition systems are needed in the DT test so as to achieve the displacement control and record the in-situ change of load P.

Furthermore, since the crack velocity can be easily overestimated due to creep, creep-induced relaxation (CR) tests are strongly recommended (Cai 2012) for DT tests. It uses DT specimens on same geometry and loading configuration but without notch. The CR tests will be performed in a similar way as a DT test with constant displacement. The measured force-time curves from CR tests will be compared with the ones obtained from DT tests. Although this is an effective way to eliminate the influence of creep, additional work is needed and it is apparently time-consuming as well.

Last but not the least, the deterioration in concrete induced by chemical attacks is usually a slow process. Therefore, to understand the kinetics of SCG (especially in Regions II and III), the time duration of the test must be long enough to allow the full development of chemo-

mechanical interaction, even when accelerated methods are used. This means the testing systems will be occupied and exposed to a corrosive condition for a long period of time.

Currently, the use of DT test (or other displacement control-based experimental methods) to investigate the SCG in cement-based materials subject to chemo-mechanical deterioration is very limited. In light of the cost of time and equipment, as well as the risk of equipment damage induced by corrosive media, the DT test is almost exclusively used to test cement-based materials under static fatigue (Evans, 1972; Williams and Evans, 1973; Swanson, 1984; Cai, 2012). For example, Cai (Cai, 2012) recently used the DT test to investigate the SCG in hardened cement pastes under static fatigue. Since only one set of testing system was available, the test for each specimen was completed within 1 hour to mitigate the effect of the age difference. However, the DT test or other experimental investigation on the SCG under stress corrosion is seldom reported in the literature for concrete. The lack of knowledge about the kinetics of SCG under stress corrosion obstructs the progress to understand the coupled deterioration processes in concrete structures during their service. Furthermore, without the information of the changes in the microstructure and chemical composition, it is extremely difficult to construct a realistic model to numerically approximate the performance of cement-based materials subject to chemo-mechanical deterioration.

To overcome these obstacles, a novel test is designed in this study to investigate the SCG in cement-based materials. Contrary to the displacement control used in the DT test, a constant load is applied to the specimens to trigger stable crack propagation in this experimental approach. Thus, many components of the sophisticated testing system required in the DT test are no longer needed.

1.1.4 Lattice Model and Numerical Simulations

As observed in the tests before (Bogue and La chimie du ciment Portland, 1952; Berner, 1988, 1992), SCG will occur in cement-based materials under a much lower load if the mechanical damage is accompanied with chemical attacks. This implies that the safety and serviceability of concrete structures may be significantly compromised by the superposition of different deterioration processes, even if each individual process alone is not critical for the structural integrity. Therefore, it is of significant importance to establish a realistic model to numerically approximate the subcritical crack growth in cement-based materials subject to chemo-mechanical deterioration for predicting the lifetime of concrete structures.

According to previous studies, a number of approaches (Gerard, Pijaudier-Cabot and Laborderie, 1998; Bangert, Kuhl and Meschke, 2001; Le Belléego, Géerard and Pijaudier-Cabot, 2001; Le Bellégo, Gérard and Pijaudier-Cabot, 2001; Le Bellégo *et al.*, 2003; Kuhl, Bangert and Meschke, 2004) have been proposed to approximate the complex interactions of mechanical damage and calcium leaching in cement-based materials. Despite the different formulation in chemical equilibrium, ion transport and damage evolution, a common idea in most of these approaches is to treat concrete as a porous medium, which is then numerically approximated by a continuous model.

For instance, in the pioneering work by Gérard et al. (Gerard, Pijaudier-Cabot and Laborderie, 1998), empirical relations and isotropic damage mechanics are used to link the skeleton damage, ion concentration, transport property and porosity variation. However, in this continuous model, the irreversibility of matrix dissolution is not guaranteed. To remedy this inadequacy, Kuhl et al. (Kuhl, Bangert and Meschke, 2004) proposed a continuous model based on the theory of mixtures (Bowen, 1976), in which a chemical reaction criterion was enforced to

prevent the reverse of skeleton decalcification. In this framework, the porosity of cement matrix is deemed as the key indicator of chemo-mechanical attacks. However, this work does not consider the SCG under a sustained load, and only the instantaneous fracture of cementitious skeleton is taken into account in the modeling. Thus, the kinetics of crack growth in stress corrosion cannot be realistically captured in this model.

In addition to the absence of crack-growth kinetics, these continuous approaches, usually anchored at isotropic damage mechanics, seldom consider the anisotropy of ion conductivity induced by the orientation of skeleton cracking. A simplified isotropic conductivity tensor is generally used in these continuous models to represent the transport property of cracked matrix. However, the stress corrosion test in this study, as well as the experimental evidence in other studies (Wang and Ueda, 2011), shows that the matrix dissolution and ion diffusion in the fracture process zone (FPZ) is not isotropic (Wang *et al.*, 2016). This is due to the fact that if a subcritical crack develops in the cement matrix, the migration rates of ions along the crack will be much faster than in other directions.

To investigate the effect of skeleton cracking on other physical processes, in particular on those related to conductivity, the use of discrete approaches has been garnering increasing interest. Unlike the continuous formulation, discrete approaches discretize a continuous medium with a system of particles or lattices. Residing on their advantages in approximating the micro- or meso-structure of a heterogeneous medium, both the particle models (Cusatis and Nakamura, 2011; Cusatis, Mencarelli, Pelessone and Baylot, 2011; Cusatis, Mencarelli, Pelessone, Baylot, *et al.*, 2011) and lattice models (Bolander and Berton, 2004; Wang and Ueda, 2011; Grassl *et al.*, 2015) are widely used for studying quasi-brittle materials including concrete and rocks. For example, Potyondy (Potyondy, 2007) used a bonded-particle model to study stress corrosion in

rocks. Although an exponential law is employed to capture the kinetics of crack growth in the particle bonds, this model does not consider any chemical equilibrium, moisture migration and ion conductivity. Recently, lattice models have been utilized to investigate the mass transport, chloride diffusion and moisture ingress in cementitious materials (Sadouki and van Mier, 1997; Wang and Ueda, 2011; Šavija, Pacheco and Schlangen, 2013). To capture the interaction between rock fracture and water pressure, Grassl et al. (Grassl *et al.*, 2015) combined two lattice systems to model the hydraulic fracture in rocks. However, despite the consideration of coupled physical processes, these lattice models do not describe the kinetics of skeleton cracking and rate of matrix dissolution. Thus, they cannot be used to predict the lifetime of concrete subject to concurrent mechanical damage and calcium leaching.

Motivated by the experimental results obtained in this study and inspired by the recent advance in modeling hydraulic fracture (Grassl, 2009), a two-dimensional (2D) discrete model consisting of two lattice systems is constructed to approximate the process of chemo-mechanical deterioration in cement-based materials. In this model, the mechanical response of material skeleton and the dissolution process of cement matrix are respectively described by two lattice systems, both of which use one-dimensional (1D) elements to discretize the same 2D domain. The damage-induced conductivity anisotropy in cement matrix can be achieved by the coupling of 1D transport element with the corresponding 1D mechanical element, for which damage mechanics is employed to approximate the skeleton cracking. This will be further expanded in Chapters 6, 7 and 8 in details.

1.2 RESEARCH OBJECTIVES

The proposed test is designed for the experimental characterization to track the SCG and to obtain the *K*-*v* curve, while a 2D lattice-based numerical framework is constructed to simulate the coupled chemo-mechanical process. The objective of the proposed study is to develop a novel test as well as construct a 2D lattice-based chemo-mechanical formulation to investigate the kinetics of SCG in quasi-brittle materials under concurrent mechanical and chemical attacks. In order to accomplish the goals, this work is focused on three major tasks:

1. To design of a novel test to investigate SCG under concurrent chemo-mechanical attack. In the test, specimens of negative geometry subject to sustained loading are immersed in an acidic solution of high concentration to mimic the concurrent chemical and mechanical attacks. To record the crack propagation as well as strain/stress distribution around the crack tip, a high-resolution microscopic system is applied to scan the specimen surface.

2. To investigate the experimental data in both macro- and micro-scales. With the benefit of the novel test, complete *K*-*v* curves can be obtained and the trends of the *K*-*v* curves are significantly different between corrosive and non-corrosive conditions (static fatigue and stress corrosion). By utilizing advanced micro-characterization techniques such as Scanning Electron Microscopy (SEM) and Atomic Force Microscopy (AFM), the mechanical and transport characteristics during the chemo-mechanical process are quantified.

3. To construct a two-way coupled constitutive law in numerical simulations. Using the experimental results as benchmark, numerical simulations based on a 2D lattice model are carried out. To capture the heterogeneity of cementitious materials at meso-scale, the specimen is mapped on a lattice system so as to separate the lattice elements representing different constituents. This mapping technique has an outstanding advantage in assigning transport

property to the lattice elements to approximate the effect of dissolution kinetics. Based on the numerical simulations, a parametric exploration is undertaken to probe the correlation between SCG kinetics and the coupled chemo-mechanical parameters.

1.3 SCOPE OF THE DISSERTATION

This thesis is organized as follows:

In Chapter 2, the specimen design is introduced. Within the framework of linear elastic fracture mechanics (LEFM), a specimen of negative geometry is determined. In Chapter 3, the static fatigue and stress corrosion test on the hardened cement pastes are described. In the test, two batches of cement paste, characterized by different water-cement ratios, are used to cast specimens. The chemical attack is focused on calcium leaching and is induced by a high-concentration acidic solution. In Chapter 4, the obtained *K*-*v* curves are presented and the kinetics of SCG in stress corrosion are compared with what observed in static fatigue. In Chapter 5, the macro- and micro-characterization of specimens experiencing chemo-mechanical deterioration are conducted by a variety of tests. In addition to the measurements of apparent porosity and decalcified area, the microstructure destruction and chemical composition change are quantified by SEM, AFM and Raman spectroscopy.

Chapter 6 is focused on modeling the coupled chemo-mechanical deterioration based on the chemical equilibrium, mass transport, kinetics of SCG and damage mechanics. To couple the matrix dissolution and skeleton damage, the fully saturated pore space in cement matrix is deemed as a time-dependent variable, whose evolution is dictated by the intertwined chemo-mechanical process. In Chapter 7, the discretization of cement matrix by two lattice systems is

described. With the aid of Delaunay tessellation and Voronoi tessellation, the 1D transport element is placed in a direction normal to the corresponding 1D mechanical element. In Chapter 8, the implementation of this 2D discrete model in ABAQUS is illustrated. To reduce the computational cost resulting from the slow deterioration process, an artificial time scale is employed to enable the use of coarse temporal discretization in the explicit formation for quasi-static analysis. In Chapter 9, simulations are conducted and numerical results are compared with results obtained in both the micro- and macro-characterization tests in Chapters 4 and 5.

Finally, some conclusions are drawn in Chapter 10 and future research is discussed.

2.0 SPECIMENS OF NEGATIVE GEOMETRY

Within the framework of LEFM, stable crack propagation in brittle materials only happens when the energy release rate G is equal to the crack growth resistance R, which is a material constant. Residing on Irwin's work (Irwin, 1958), the relation between G and K can be expressed as:

$$G = \frac{K^2}{E'} = \frac{P^2}{\delta^2 D E'} f(\alpha) \tag{5}$$

where E' is the effective modulus of a given homogeneous material, D is the characteristic size of specimen, δ is the specimen thickness, P is the applied load, $\alpha = a/D$ is the relative crack length (a dimensionless value), and $f(\alpha)$ is a dimensionless function dependent only on the specimen geometry.

Equation (5) implies that for a given homogeneous specimen, G will be governed by $f(\alpha)$ when P is a constant. Therefore, to achieve stable crack propagation under a constant load, $f(\alpha)$ cannot increase with crack growth. Otherwise, G will be greater than R after fracture is initiated, which inevitably leads to dynamic crack propagation. Thus, to use load control in stress corrosion or static fatigue test, $f(\alpha)$ must decrease with α. Usually, specimens of this property are called specimens of negative geometry (Bazant and Planas, 1998).

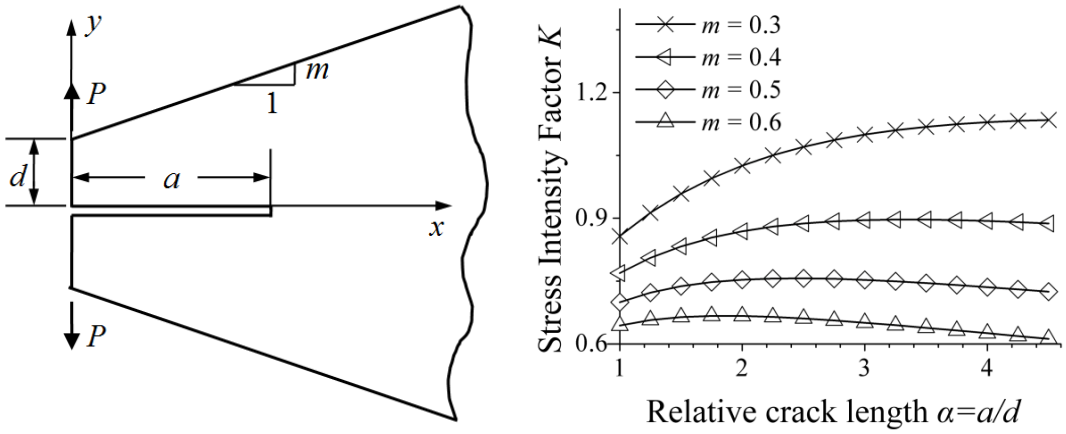

Figure 6. (a) An infinite trapezoidal strip based on Tada's handbook (Tada et. al 2000), and (b) the dependence of K on α for different slopes m

To find the suitable negative geometry, an infinite plate of trapezoidal shape selected from Tada's handbook (Tada, Paris and Irwin, 2000) is explored (Figure 6a). In mode-I fracture, K at the crack tip can be approximated by an empirical function (Tada, Paris and Irwin, 2000):

$$K = \frac{P}{\delta\sqrt{D(1+m\alpha)}}\left(3.46-2.65m+1.89^{3/2}\right)\left(\frac{\alpha}{1+m\alpha}+0.7\right) \tag{6}$$

The dependence of K on α is plotted in Figure 6b. The figure shows if m is not less than 0.5 and α is greater than 1.5, K will decrease with crack propagation. In view of this, a trapezoidal plate is designed for the test. The dimensions of the specimen are shown in Figure 7. Based on Figure 6b, m = 0.6 is selected for the side edges.

The supports and loads are symmetrically applied, as shown in Figure 7, to generate a mode-I fracture. Since the loading and support conditions are different from the infinite plate in Tada's handbook (Tada, Paris and Irwin, 2000), Eq. (6) is no longer effective for the designed

specimen. Thus, the dependence of K on a is numerically calculated by finite element analysis in ABAQUS. The obtained curves in Figure 8 show that if crack length a is within the range from 30 to 85 mm, the specimen is of negative geometry. Thus, the notch length in the specimens is designed to be 30 mm.

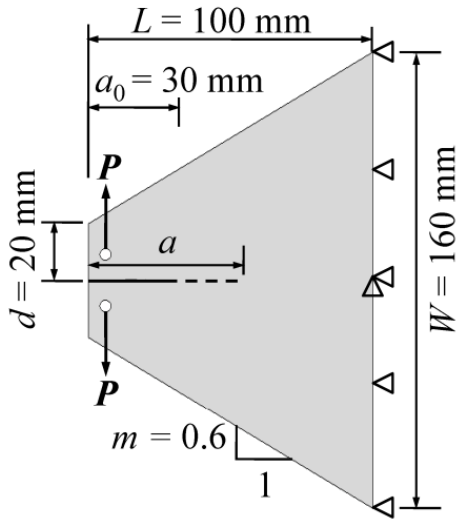

Figure 7. Illustration of the specimen geometry and loading configuration

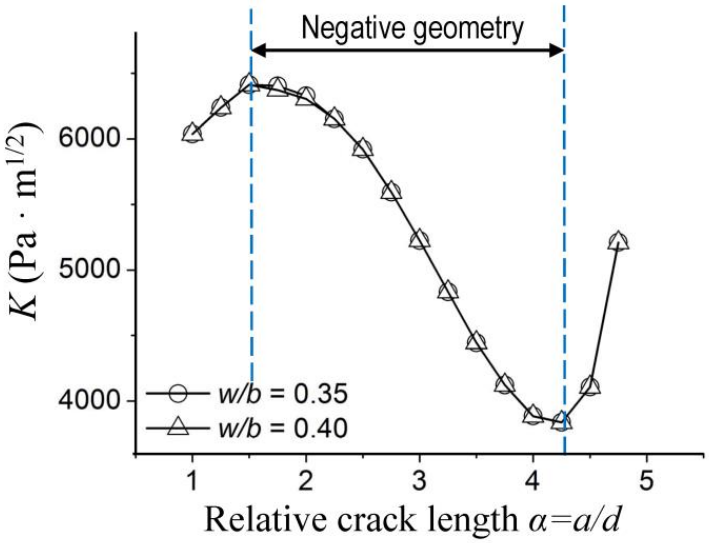

Figure 8. The numerically obtained K-α curves for different w/b ratios under unit load

3.0 EXPERIMENTAL TESTING

After the dimension and shape are determined in Chapter 2, the specimens are cast with Type I Portland cement. Two batches of hardened cement paste, characterized by the water-cement ratios (*w/b*) of 0.35 and 0.40 respectively, are used in this test. The reasons for using hardened cement pastes without any aggregates are 1) to make the specimens more brittle and 2) to eliminate the disturbance induced by the interfaces between aggregates and cement pastes. No admixtures are added. The cement paste is stirred for 1 min in a Hobart mixer at low speed and then stirred for 2 more min at high speed after a 15-second pause. Now, the well-stirred cement paste is poured into the specially designed moulds made of polymethyl methacrylate (PMMA) to cast nine trapezoidal plates. Wax and oil are applied to the moulds before casting to ease demolding. In addition, for each batch of the mixture, three small prisms, three cylinders and three edge-notched beams are cast at the same time. All the moulds with cement paste inside are placed on a vibrator for more than 5 min at intermediate vibration to avoid large air bubbles. Then the moulds are covered with plastic wrap thoroughly to prevent moisture loss. After 24 hours, all of these specimens are carefully taken out from the moulds and cured under standard conditions (99% relative humidity and about 20°C) before they are tested.

3.1 MATERIAL PROPERTY TEST

In addition to the trapezoidal plates for stress corrosion and static fatigue tests, cylinders, prisms and edge-notched beams cast from the same batch are used to probe the material properties of hardened cement paste. The dimensions of the specimens are shown in Figure 9 and the arrangement of tests are listed in Table 1.

For each trapezoid thin-plate specimen, a 5 mm wide × 3 mm deep × 100 mm long guiding groove in the middle along the centerline is generated by the specially designed moulds. Before testing, a 3 mm wide × 3 mm deep × 30 mm long notch is cut at one end of the specimen, as shown in Figure 7. Each trapezoid specimen is roughly ground on grit-40 sand paper and then finely ground on grid-400 sand paper to polish its surface. Then three layers of anti-corrosion coating are uniformly applied to the surface of the specimen. After that, a tapered pre-crack is cut by a razor blade at the notch tip to promote crack initiation as recommended by Cai's work (Cai, 2012). With the help of coating and pre-cut initial crack, chemical species from the corrosive solution can only attack the crack tip and spread through the cracked surface without penetrating inside from the other parts of the thin-plate specimen.

For each batch of the mixture, three cylinders with standard dimension of 4 in. diameter × 8 in. height (102 mm diameter × 203 mm height) are cast and then cured for 28 days before the axial compression test. The test follows the ASTM recommendations (C39/C39M-15) (Standard, 1997) and the obtained average compressive strength $f_c^{'}$, elastic modulus E and Poisson's ratio v are given in Table 2.

Similarly, for each edge-notched beam, a 3 mm wide × 23.3 mm deep × 30 mm thick notch is cut in the middle of it. The three edge-notched beams are tested under 3-point bending

after 28-day curing. Based on the test results, the estimated tensile strength $f_t^{'}$ and fracture energy G_f in terms of the cohesive crack model (in which a linear softening law is used) are listed in Table 2. The obtained fracture energy agrees with a recent study on cement pastes (Xu and Zhu, 2009).

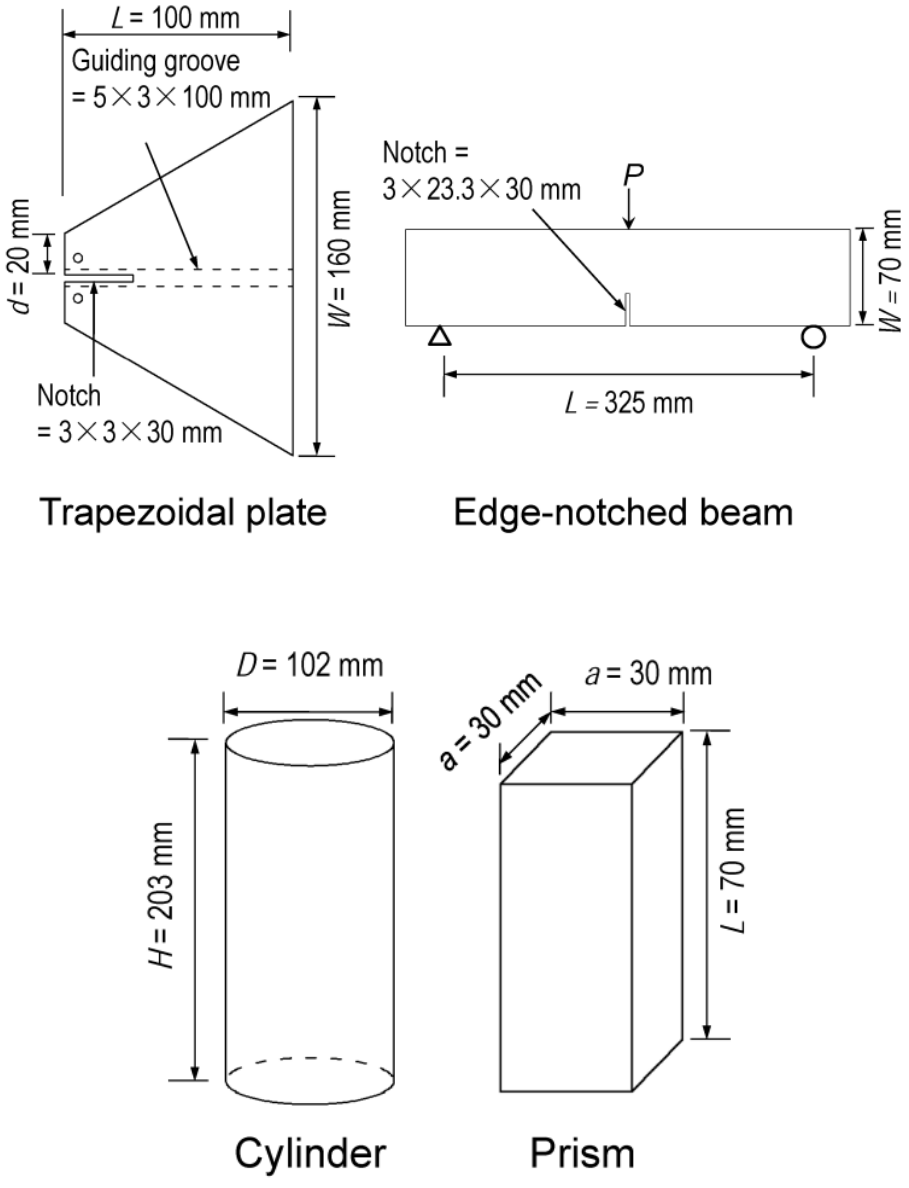

Figure 9. Dimensions of specimens used in the test

Moreover, the three prisms from each batch are designed to be immersed in the same acidic solution with the corresponding trapezoidal plates undergoing stress corrosion. In order to approximate uniform calcium leaching along one direction, several layers of anti-corrosion paint is sprayed on all the surfaces of each prism except one end. By examining the decalcified areas in the prisms, the deterioration process induced by calcium leaching alone is probed. The results of deterioration development are shown in Chapter 5.1.

Table 1. An overview of the designed tests (the numbers denote number of tests on different specimens)

Test Name	Specimen	Number	*w/b* ratio
Static fatigue test	Trapezoidal plate	3	0.35
		3	0.40
Stress corrosion test	Trapezoidal plate	6	0.35
		6	0.40
Three-point bending test	Edge-notched beam	3	0.35
		3	0.40
Axial compression test	4 in. diameter by 8 in. height cylinders	3	0.35
		3	0.40
Decalcification test (Phenolphthalein test)	Prism	3	0.35
		3	0.40

Table 2. Material properties of the hardened cement pastes

Property		*w/b* = 0.35	*w/b* = 0.40
Compressive strength	$f_c^{'}$	45.13 MPa	45.00 MPa
Tensile strength	$f_t^{'}$	4.20 MPa	4.00 MPa
Fracture energy	G_f	21.00 N/m	18.00 N/m
Young's modulus	E	23.00 GPa	17.80 GPa
Poisson's ratio	v	0.29	0.26

3.2 STRESS CORROSION AND STATIC FATIGUE TESTS

Among the nine trapezoidal plates of negative geometry in each batch, six of them will be used for the stress corrosion test and the other three for the static fatigue test. To direct the crack propagation, a 5 mm-wide guiding groove similar to the DT test is adopted in the trapezoidal plates. To comply with the 2-dimensional analysis in the finite element model (FEM model), as well as to ensure a uniform crack tip, the thickness of plates is selected to be 6 mm and it is reduced to 3 mm within the guiding groove.

A frame made of PMMA, which is inert in acidic solutions, is built for each plate. The plate is placed on the frame and supported by four cylindrical rollers made of stainless steel so that it can move freely in the transverse direction (Figure 10a). The end of the plate is supported on a stopper so that any movement in the direction along the crack is resist, as illustrated in Figure 7. One steel block is hung on each side of the notch through a pulley so as to apply the

load *P*; see Figure 10a. Since the plate is lightweight, the frictional forces of the rollers to resist *P* are negligible. To protect the steel blocks from corrosion, anti-corrosion paint is sprayed and anti-corrosion tape is used to wrap the blocks. In addition, the force *P* is frequently checked by the spring-type sensors during the tests.

(a) (b)

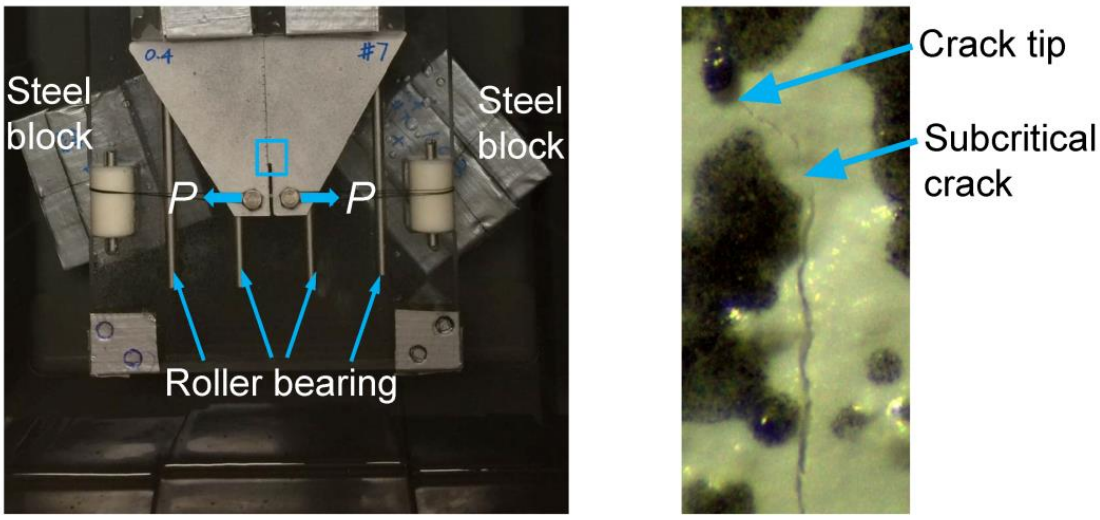

Figure 10. (a) Top view of the experimental setup for stress corrosion and static fatigue tests, and (b) a subcritical crack captured in the microscopy system

To trace the crack propagation in a plate, a microscopy system, with the resolution up to 1 μm, is employed to identify the crack tip on the plate surface (Figure 10b). SCG will develop continuously along the center line of the specimen. When the crack tip develops from one location to a new one, the crack advance can be obtained and the average crack velocity is calculated. By tracking the crack evolution, a series of points can be acquired to form a complete *K*-*v* curve from one test. Apparently, the higher frequency of observation it is, the smaller the time interval will be and more smooth curves can be achieved for the complete *K*-*v* curve.

In the stress corrosion test, six trapezoidal plates from each batch, together with the frames and steel blocks, are immersed in an acidic solution, which causes calcium leaching in the hardened cement pastes. To accelerate the decalcification and dissolution process, an ammonium nitrate solution (NH_4NO_3) of 10% concentration is used in the stress corrosion test. To isolate the chemo-mechanical interaction, three layers of anti-corrosion paint are sprayed on all the surfaces of every plate, except for the notch surfaces and notch tip. Therefore, the chemo-mechanical attack induced by calcium leaching and the load P can only start from the notch tip and penetrate into the specimen from the crack. The applied load P is 26.8N for the batch of w/b = 0.35 and 26.5N for w/b = 0.40. Note that these loads are determined based on a series of trial tests and the results of edge-notched beam test.

Three trapezoidal plates from each batch serve as the static fatigue test (also is the control group). The setup is similar to the stress corrosion test while only differences are that 1) the trapezoidal plates are immersed in clean water and 2) the load P is increased to 35.8N for the batch of w/b = 0.35 and 35.4N for w/b = 0.40. To avoid calcium leaching in clean water, calcium hydroxide is added to the water until it reaches the saturation level.

Both of the stress corrosion and static fatigue tests start at the same time. The specimens are under standard curing for 55 days before testing. Since the specimens are immersed in an acidic solution or clean water, the effect of drying shrinkage, which may cause tensile cracking to disturb the SCG in thin specimens, is eliminated. By tracing the location of the crack tip, the stress intensity factor K is calculated based on the curves in Figure 8, and the crack velocity v is calculated as an averaged value based on the crack length difference between two subsequent measurements and the corresponding time interval, as introduced before.

In the test, the crack tip observed in the microscopy system is the nominal crack tip. Note that cement-based materials are not perfectly brittle. Instead, they are archetypical quasi-brittle materials characterized by a non-negligible fracture process zone (FPZ) ahead of the nominal crack tip (Bazant and Planas, 1998). Therefore, for hardened cement pastes, the use of Eqs. (5) and (6) should be in the context of equivalent LEFM, in which the nominal crack is replaced by an equivalent crack with its tip located inside the FPZ. The location of this equivalent crack tip, which cannot be accurately determined by the conventional optical methods, may be estimated by measuring the crack mouth opening, similar to measuring the compliance of specimens in the DT test.

However, in this test, the crack mouth opening is not measured and only the nominal crack tip is traced. One reason is that during stable crack propagation, it is a rational approximation to assume that the distance between the nominal crack tip and equivalent crack tip will not change. Thus, the trend observed in the K-v curve based on the nominal crack tip should be similar to that based on the equivalent crack tip. Moreover, the material property of plates subject to chemo-mechanical deterioration will change over time and this change is not uniform within the specimens due to the nonlinear interaction between mechanical damage and calcium leaching. This means the specimens can no longer be treated as plates made of homogeneous and isotropic materials after calcium leaching. For these plates, crack mouth opening alone is not sufficient for identifying the equivalent crack tip. The evolution of modulus distribution within a specimen is needed, which unfortunately is unknown prior to the test and difficult to measure during the test. Therefore, to have a common ground for the comparison of SCG between stress corrosion and static fatigue, the nominal crack tip is used in this experimental investigation.

3.3 CRACK TIP VALIDATION

Since the crack tip is detected through a microscopy system scanning the surfaces of the specimens, the crack tip inside a specimen is not accessible. To ensure the crack propagation is uniform along the specimen thickness and the use of microscopy system is appropriate, three specimens at different test stages were randomly selected and then examined by a 3D computed tomography (CT) scan system, which is of a resolution up to 11.7 μm, sufficient for identifying the micro- and meso-cracks in hardened cement pastes.

Based on the dimension requirement of this CT scan system, a strip of hardened cement paste containing the guiding groove is cut out from the selected specimen. In the examination, 510 scans are conducted along each principal direction for each sample. Based on the images obtained in the 3D CT scan (Figure 11), it is found that the difference between the crack tip locations found in the CT scan and microscopy system is only about 1.93%, 3.80% and 2.24% of the crack length in the three samples, respectively. This negligible difference means that the crack propagation is almost uniform in the thin plates and it is acceptable to use the crack tip identified on the specimen surface by the microscopy system.

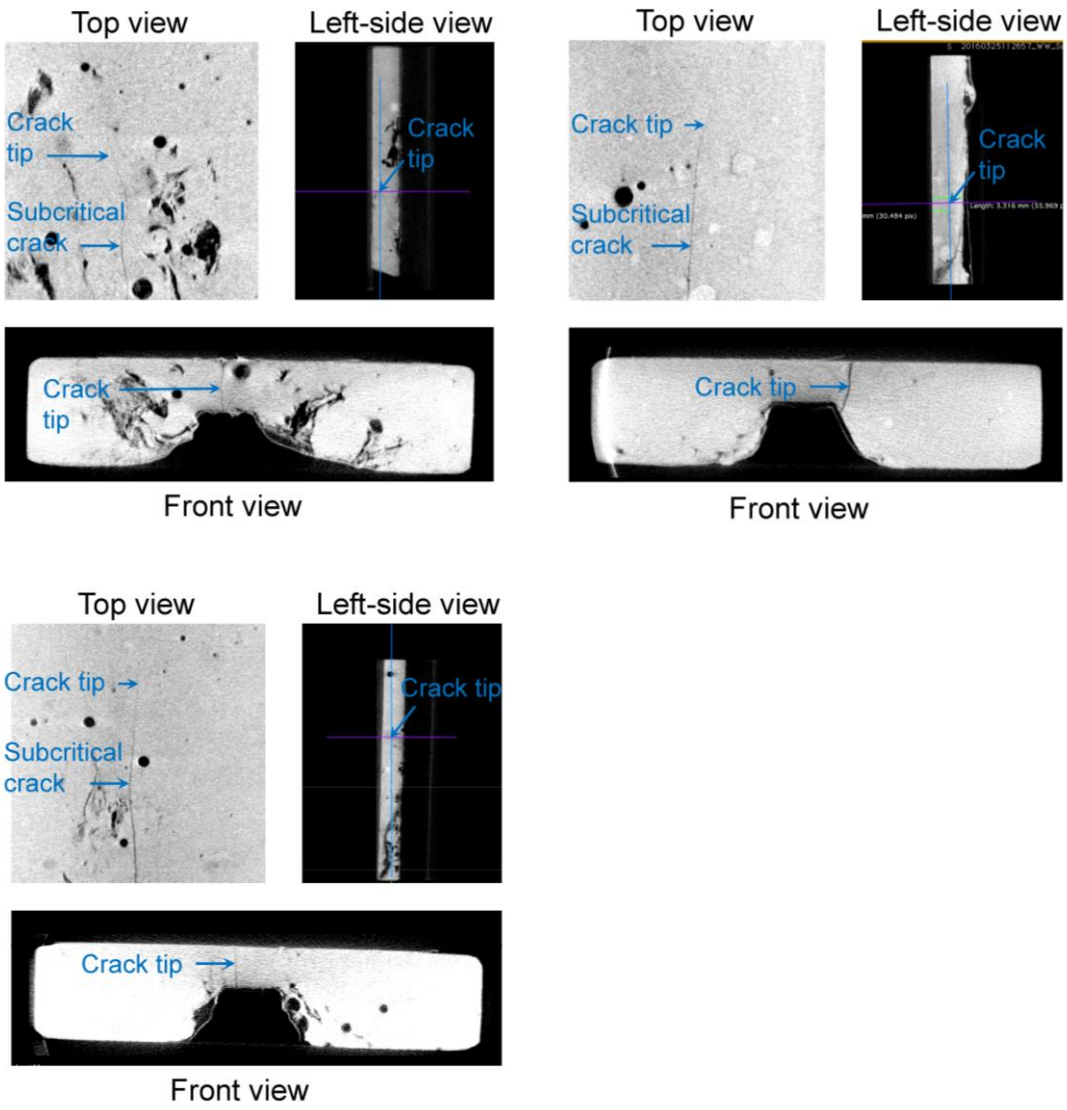

Figure 11. The crack tip identified in a 3D CT-scan system

4.0 OBTAINED *K*-*V* CURVES

For the trapezoidal plates immersed in water (the static fatigue test), the test lasts 66 days. The advance of the nominal crack tip with time is plotted in Figure 12 for the two batches of different water-cement ratios (w/b = 0.35 and 0.40, respectively). The corresponding *K*-*v* curves are depicted in Figure 12, too. Similar to the findings by other researchers, the obtained *K*-*v* curves of SCG under static fatigue are almost straight lines in the double-logarithmic scale.

For specimens of w/b = 0.35, the average slope of the *K*-*v* curves is 709.42 (with a standard deviation s = 42.26) in the double-logarithmic scale; while for w/b = 0.40, the average slope is 457.82 (with s = 113.6). Compared with the results by Cai (Cai, 2012), who used the DT test to investigate the SCG in hardened cement pastes under static fatigue, the slopes obtained in this study are realistic. If the crack velocity $v_0 = 10^{-10}$ m/s is selected as the threshold for crack propagation, the corresponding threshold stress intensity factor K_0 is about 2.28×10^5 Pa·m$^{1/2}$ for the specimens of w/b = 0.35. This means if the K induced by external loads is less than K_0, the SCG cannot be observed in this hardened cement paste. For w/b = 0.40, K_0 is close to 2.24×10^5 Pa·m$^{1/2}$. This indicates that for a weaker hardened cement paste, the SCG will start under a lower load.

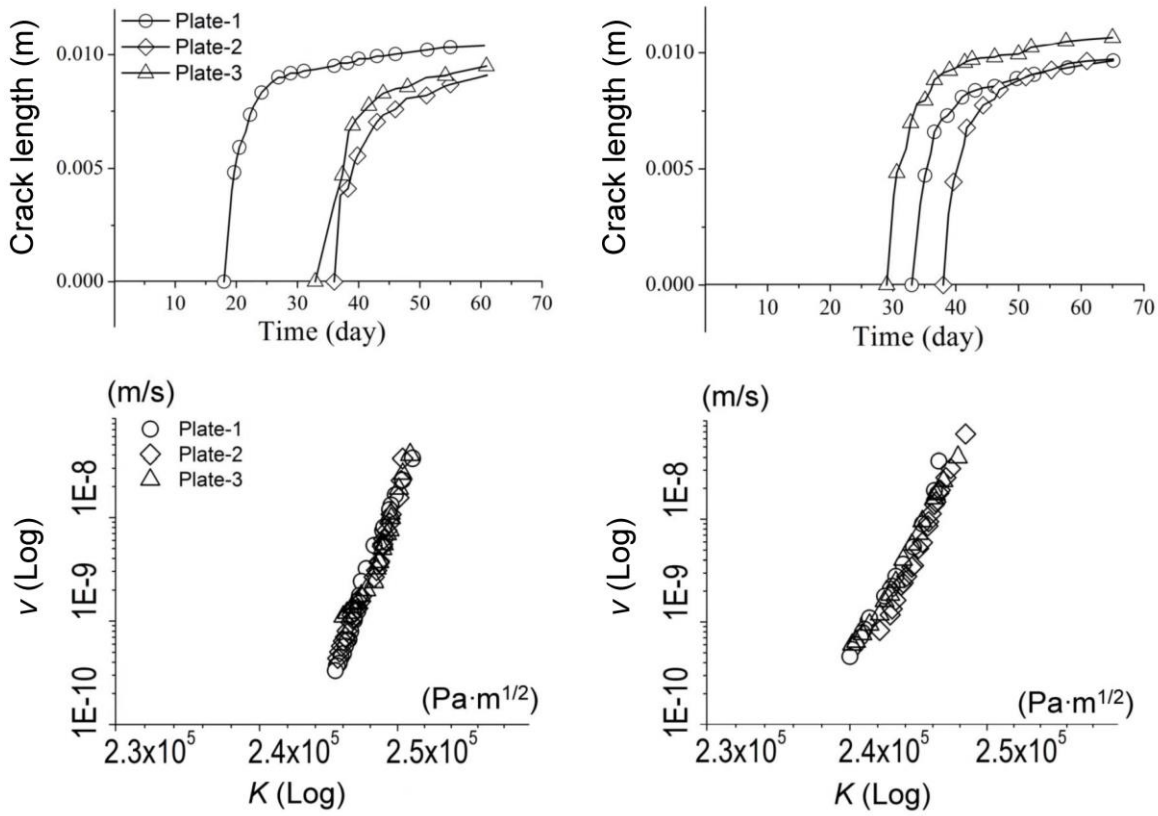

Figure 12. Advance of crack tip with time and the corresponding *K*-*v* curves for the specimens under static fatigue: (left) *w*/*b* = 0.35, and (right) *w*/*b* = 0.40

The stress corrosion test lasts 89 days. Among the six plates from each batch, two of them are sacrificed during the test for macro- and micro-characterization. The advance of the nominal crack tip with time is shown in Figure 13 for the two groups of specimens, where the sacrificed plates are labeled as Plates 5 and 6 respectively. Different from the static fatigue test, the *K*-*v* curves based on the nominal crack tip are no longer straight lines in the double-logarithmic scale. Instead, the general trend of SCG is comprised of three distinctive regions (I, II and III); see Figure 13. The SCG in these three regions agrees quite well with the trend capture in other materials (e.g., soda-lime glass subject to stress corrosion (Wiederhorn, 1967; Wiederhorn *et al.*, 1982)).

In Region I, the curves show steeper slopes than in the other two regions. The average slopes for w/b = 0.35 and 0.40 are 330.04 and 193.13 (with s = 99.16 and 43.44) respectively. These slopes are comparable to those observed in the static fatigue test. This means the stress intensity factor induced by P plays a dominant role in the rate of crack growth.

However, in Region II, the curves turn to be almost flat and the average slopes are significantly reduced to 24.63 (with s = 4.71) for w/b = 0.35 and 25.61 (with s = 11.91) for w/b = 0.40. This indicates the role of stress intensity factor is no longer significant. The crack velocity is limited by the transport rate of reactive chemical species from the surrounding environment to the crack tip. Thus, the decalcification and dissolution process play a more important role in this stage.

In Region III, the slopes of K-v curves become steeper again, although they are still less than those in Region I. The average slopes for w/b = 0.35 and 0.40 are 132.17 and 78.10 (with s = 51.54 and 15.24) respectively. In this stage, the strength of paste at crack tip is significantly weakened by the chemical attack induced by the corrosive species. Therefore, environmental-assist deterioration process around the crack tip dictates the crack propagation. In other words, the role of stress intensity factor K is enhanced in the crack growth by the decalcification and dissolution process.

Based on the slopes in Region III, the threshold stress intensity factor K_0 can be estimated for the hardened cement pastes subject to chemo-mechanical deterioration. For w/b = 0.35, the average slope leads to $K_0 = 1.60\times10^5$ Pa·m$^{1/2}$; while for w/b = 0.40, $K_0 = 1.57\times10^5$ Pa·m$^{1/2}$. Both thresholds are significantly reduced in comparison with their counterparts in the static fatigue test. This means with the aid of calcium leaching, SCG can happen in hardened cement pastes at a much lower load.

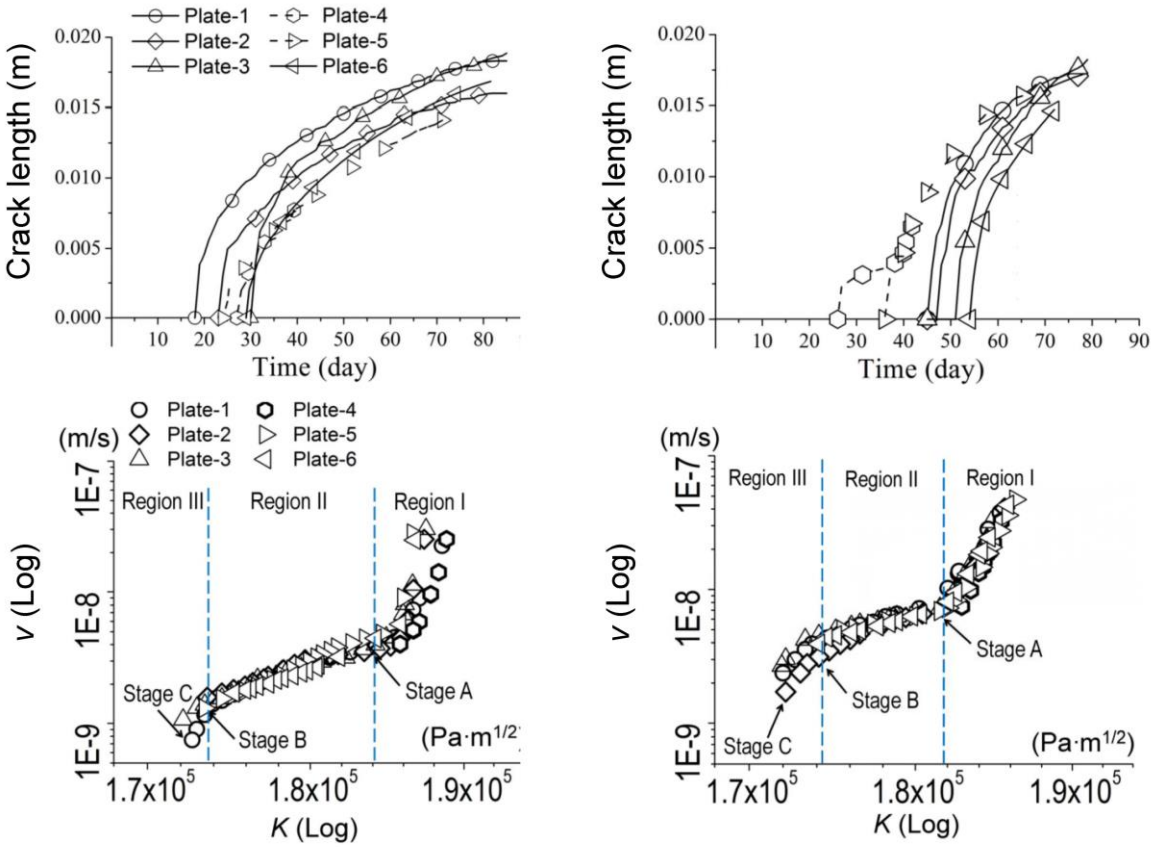

Figure 13. Advance of crack tip with time and the corresponding *K*-*v* curves for the specimens under stress corrosion: (left) *w*/*b* = 0.35, and (right) *w*/*b* = 0.40

5.0 MACRO- AND MICRO-CHARACTERIZATION

The initial mechanical properties of the cement pastes have been obtained and listed in Table 2. Monitoring the changes of these properties will provide critical benchmarks for understanding the fundamental mechanisms of chemo-mechanical deterioration. Unfortunately, since the specimens are very thin, it is extremely difficult to cut samples from the specimens subject to stress corrosion and then test the changes of compressive strength, tensile strength and fracture energy. To circumvent this obstacle, an alternative approach based on the macro- and micro-characterization is adopted.

For each batch of specimens under stress corrosion, three plates are removed from the test frames after 42-, 72-and 89-day testing (Stage A, B and C), respectively. When the *K*-*v* curves show the trend of transition from Region I to Region II, a plate and a prism from the same batch are removed from the acidic solution. When the curves start to enter Region III, another plate and another prism from the same batch are removed. At the end of Region III, one plate and the last prism are taken out. Utilizing these samples, the macro-characterization is carried out to investigate the dissolution development and porosity change.

After the macro-characterization, the samples are cut into small blocks for the micro-characterization. The small blocks are embedded into epoxy resin to prepare for the Raman spectroscopy, SEM and AFM characterization. The Raman scan is conducted first. After that, the samples are dried under 40°C for 24 hours to eliminate the disturbance of surface moisture. Then

the conventional SEM sputter coating (gold-palladium) is bombarded under a low vacuum environment (about 0.05~0.1 mbar) to the cement paste surface before SEM imaging. In the preparation for AFM nanoindentation, the surfaces of samples are carefully polished. The AFM scan using contact mode is carried out within a selected region with a size of 30×30 μm. The selected region is mapped by a grid consisting of 7×7 nodes, and the microstructural mechanical property of this region is quantitatively probed by nanoindentation at every node of this grid.

5.1 DEVELOPMENT OF DECALCIFICATION AND DISSOLUTION

To reveal the process of decalcification and dissolution induced by calcium leaching, the anti-corrosion paint is carefully removed from the trapezoidal samples. The accompanied prismatic samples are cut into half along their centerlines to expose their interior regions. Afterwards, a phenolphthalein solution, which is widely used to characterize the decalcification and dissolution in cement-based materials (Nguyen *et al.*, 2007), is applied to the surface of the specimen. On intact cement pastes which are highly alkaline, the phenolphthalein solution will turn magenta. While for severely decalcified regions of cement pastes, the phenolphthalein solution will become colorless.

The development of decalcification in the trapezoidal plates under stress corrosion is documented in Figure 14, where the nominal crack tip of each plate is marked out with a dashed line to compare with the decalcification front demonstrated by a solid line. For the prisms without loading, the development of decalcification is also reported in Figure 14, where the front of decalcified area in a prism is shown with a solid line. It can be seen that in both trapezoidal and prismatic samples, the decalcification rate in the cement paste of w/b = 0.40 is higher than

that of *w/b* = 0.35. This agrees with the general conception that higher water content leads to a more porous microstructure of cement matrix, and thus greater ion conductivity.

Although the calcium leaching starts at the same time, the decalcification develops much quicker in the trapezoidal plates than in the prisms. This is evidenced by the comparison of decalcification fronts at different stages shown in Figure 14. It indicates the external loads help the chemical attack in the chemo-mechanical deterioration process. One thing needs to be mentioned is that in the trapezoidal plates, it is found that the decalcification process is not isotropic. Instead, due to the existence of many microcracks in the FPZ ahead of the crack tip, the conductivity of cement matrix is much greater along the crack than in other directions. Thus, the decalcification front advances much quicker along the crack than in the direction normal to the crack (Figure 14).

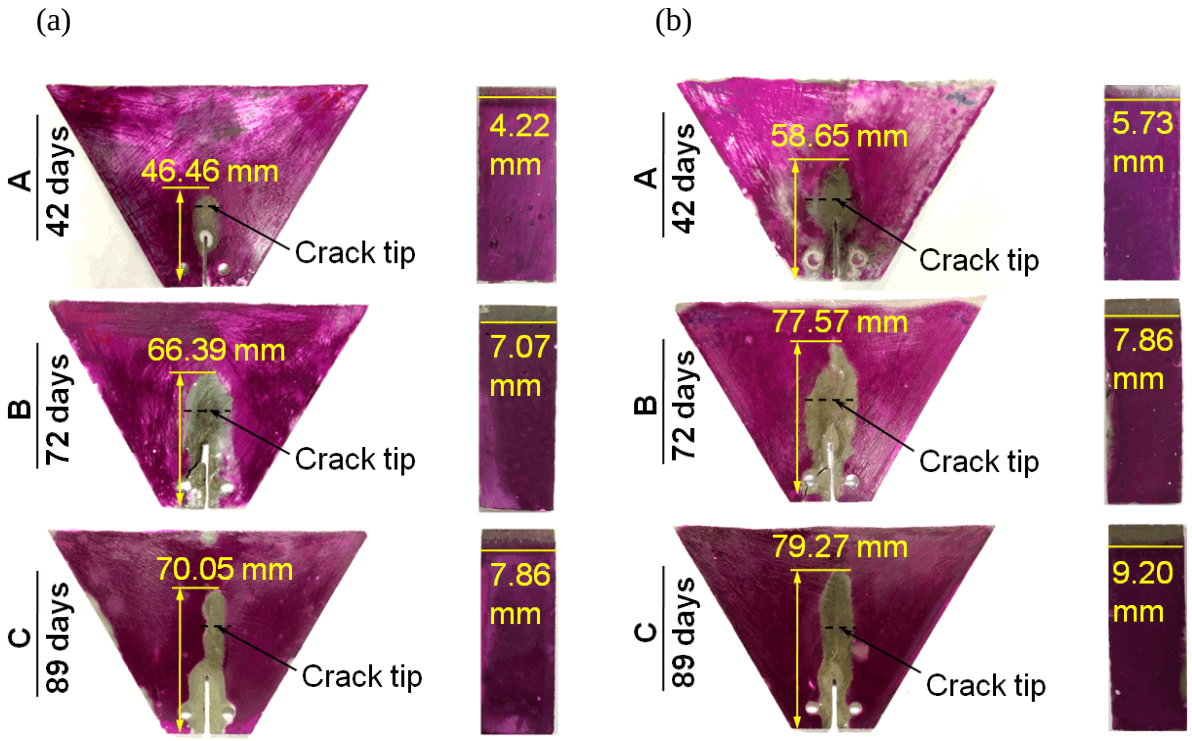

Figure 14. Decalcification development observed in the trapezoidal plates and prisms at different stages: (a) *w/b* = 0.35, and (b) *w/b* = 0.40

5.2 POROSITY CHANGE

In order to investigate the change of porosity, four representative regions are selected in each trapezoidal sample to examine the apparent porosity of cement paste at different stages of stress corrosion. The representative regions are labeled as Regions V, F, T and N, which represent the cement pastes away from the decalcification front (V), at the decalcification front (F), around the nominal crack tip (T) and at the vicinity of notch tip (N), respectively (Figure 15a). In each representative region, a small block with dimensions about 3×3×6 mm is cut out and then tested under the guide of ASTM recommendation (C948-81) for the apparent porosity of concrete (ASTM, 2000).

The obtained apparent porosity in Regions V, F, T and N is plotted in Figure 15b for Stage A. It shows that the apparent porosity of intact cement paste is about 42.12% for *w/b* = 0.35 and 42.85% for *w/b* = 0.40. Considering the material randomness of cement pastes, the measured apparent porosity is consistent with the intact cement pastes at Stage B (Figure 15c) and Stage C (Figure 15d). Note that the apparent porosity includes the nano-pores in the hydration gels, which usually play a negligible role in the ion conductivity of cement matrix.

Due to the matrix dissolution, the apparent porosity of cement pastes increases significantly. The growth of apparent porosity seems to be related to the duration of calcium leaching. At Stage A, the apparent porosity is 47.97% for *w/b* = 0.35 and 48.00% for *w/b* = 0.40 in Region F, where the decalcified area meets the intact cement matrix. The apparent porosity in Region T rises to 52.89% for *w/b* = 0.35 and 54.90% for *w/b* = 0.40. In Region N, where the cement paste endures the longest calcium leaching, the apparent porosity is increased to 55.41% for *w/b* = 0.35 and 59.77% for *w/b* = 0.40. The growth of porosity continues and the measured apparent porosity for Stages B and C is plotted in Figure 15(c, d). Note that Figure 15 shows that

the apparent porosity for cement paste of *w/b* = 0.40 is always greater than that of *w/b* = 0.35. This further supports the greater conductivity found in the decalcification process in the cement paste of *w/b* = 0.40.

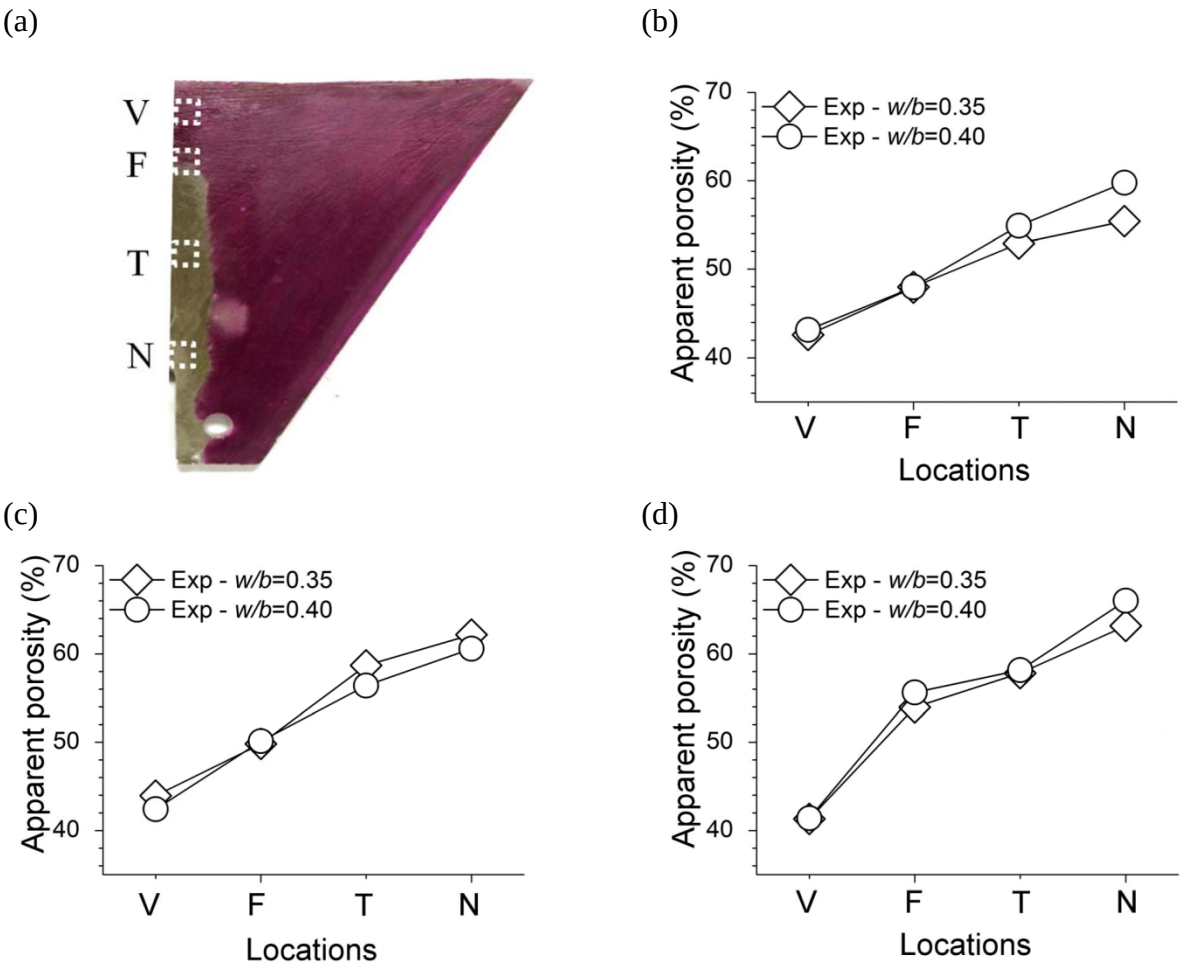

Figure 15. (a) The representative regions in the trapezoidal plate; the measured apparent porosity at (b) Stage A; (c) Stage B; and (d) Stage C

5.3 RAMAN SPECTROSCOPY MEASUREMENT

To characterize the change of chemical composition induced by calcium leaching, Raman spectroscopy is utilized to scan the samples obtained in Regions V, F and T at Stage A. During the Raman scan, the samples are usually illuminated with a laser in the near ultraviolet, visible, or near infrared range. The incident laser interacts with molecules in the samples, resulting in the energy of laser photons being shifted up or down. The shift of energy, called Raman shift (with a unit of cm^{-1}), provides information about the vibrational modes of a specific molecule (Hazle *et al.*, 1990; Potgieter-Vermaak *et al.*, 2006; Potgieter-Vermaak, Potgieter and Van Grieken, 2006). Utilizing the unique energy shift of each molecule, Raman spectroscopy is able to chemically identify the compounds of a sample.

In this test, a Renishaw Invia micro-Raman spectrometer with a Renishaw CCD detector is employed and the samples are illuminated with a 633 nm He-Ne Laser (Renishaw RL 633 laser). Chemical scan is performed by using the synchro-mode from 400 to 2100 cm^{-1}. The exposure time for each scan is 10 seconds and it takes 40 to 60 seconds to acquire one spectrum. A 50× magnification objective is used for the scan and the laser spot has a diameter of 4 μm. Before each scan, calibrations are conducted by utilizing the 520.5 cm^{-1} line of a silicon wafer.

For each region, three scans are performed at three randomly selected locations. The typical Raman spectra obtained in each region are plotted in Figure 16. It should be noted that in addition to chemical composition, the intensity of spectrum peaks also indicates the concentration of compounds. The details of peak assignment for each chemical ingredient in cement pastes can be found in the recent studies (Liu, Sun and Qi, 2014, 2015).

(a) (b)

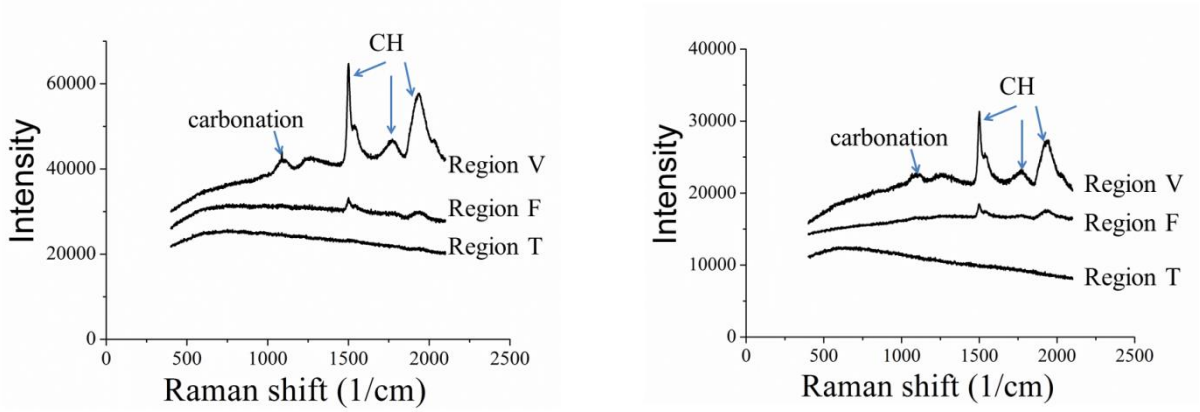

Figure 16. Raman Spectra of Regions V, F and T at Stage A for samples of: (a) *w/b* = 0.35, and (b) *w/b* = 0.40

For the intact cement paste in Region V, a group of strong peaks, ranging from 1400 to 2000 cm^{-1}, are found in the spectra for both *w/b* = 0.35 and 0.40. They indicate a significant amount of calcium hydroxide (CH) phase exists in the virgin cement matrix. The strong peak at 1086 cm^{-1} belongs to calcite ($CaCO_3$), which always coexists with the CH peaks. This coexistence is due to the fact that CO_2 in the air can be quickly dissolved in the surface moisture of cement pastes and react with the CH phase. Although the Calcium-Silicate-Hydrate (C-S-H) phase is the major hydration product that accounts for about 60% of the total volume of a hydrated paste, its peak is not detected in the spectra. The reason is that the C-S-H phase is amorphous and the C/S ratios of C-S-H gels vary over a wide range, which makes the chemical identification a very difficult task in the Raman scan (Machovic *et al.*, 2006).

In Region T, the cement paste is severely leached. This is documented by the Raman spectra in Figure 16. For both *w/b* = 0.35 and 0.40, the CH and calcite peaks entirely vanish. This indicates that the CH phase has been totally dissolved into the pore fluid. In Region F, some CH peaks can still be seen in the spectra, but their intensity is significantly decreased when compared

with that of intact cement paste. This means there is still a small amount of CH phase at the decalcification front in the cement paste.

5.4 SEM TEST

In the SEM scan, secondary electron image (SEI) technique is used to obtain the contrast image of the microstructure of cement pastes. With the aid of SEI technique, the morphology and surface topography of cement pastes can be qualitatively probed. The contrast images reflecting the surface topography under the SEI technique is realized by the so-called edge effect. More secondary electrons will leave the sample at edges and thus lead to a brighter color. In this study, a JSM6510LV SEM system is used to obtain the contrast image. During the operation, the SEM spot size is SS50 and the acceleration voltage is set at 20kV.

The SEI scan is performed in the Regions V, T and N at Stage C. The SEI images with magnification of 500 and 2500 for these three regions are shown in Figure 17, respectively. Note here only the images for samples of w/b = 0.35 are presented because the images of w/b = 0.40 show similar morphology and topography. In Figure 17a, it can be seen that although some pores and micro-cracks exist in the virgin cement matrix, the majority of microstructure surface is relatively smooth. While in Figure 17b, both the quantity and size of pores are significantly increased in Region T and the microstructure surface is no long smooth. At a magnification of 2500, the pores and micro-cracks generated by chemo-mechanical deterioration are conspicuous. For the cement matrix in Region N, which has experienced the longest calcium leaching, the SEI images show that severe microstructure destruction has happened. More pores and micro-cracks appear in the matrix microstructure. The coalescence of micro-cracks is observed at a

magnification of 500. At a magnification of 2500, it can be seen that the matrix microstructure is severely damaged and the decalcification of material skeleton generates many irregular particles.

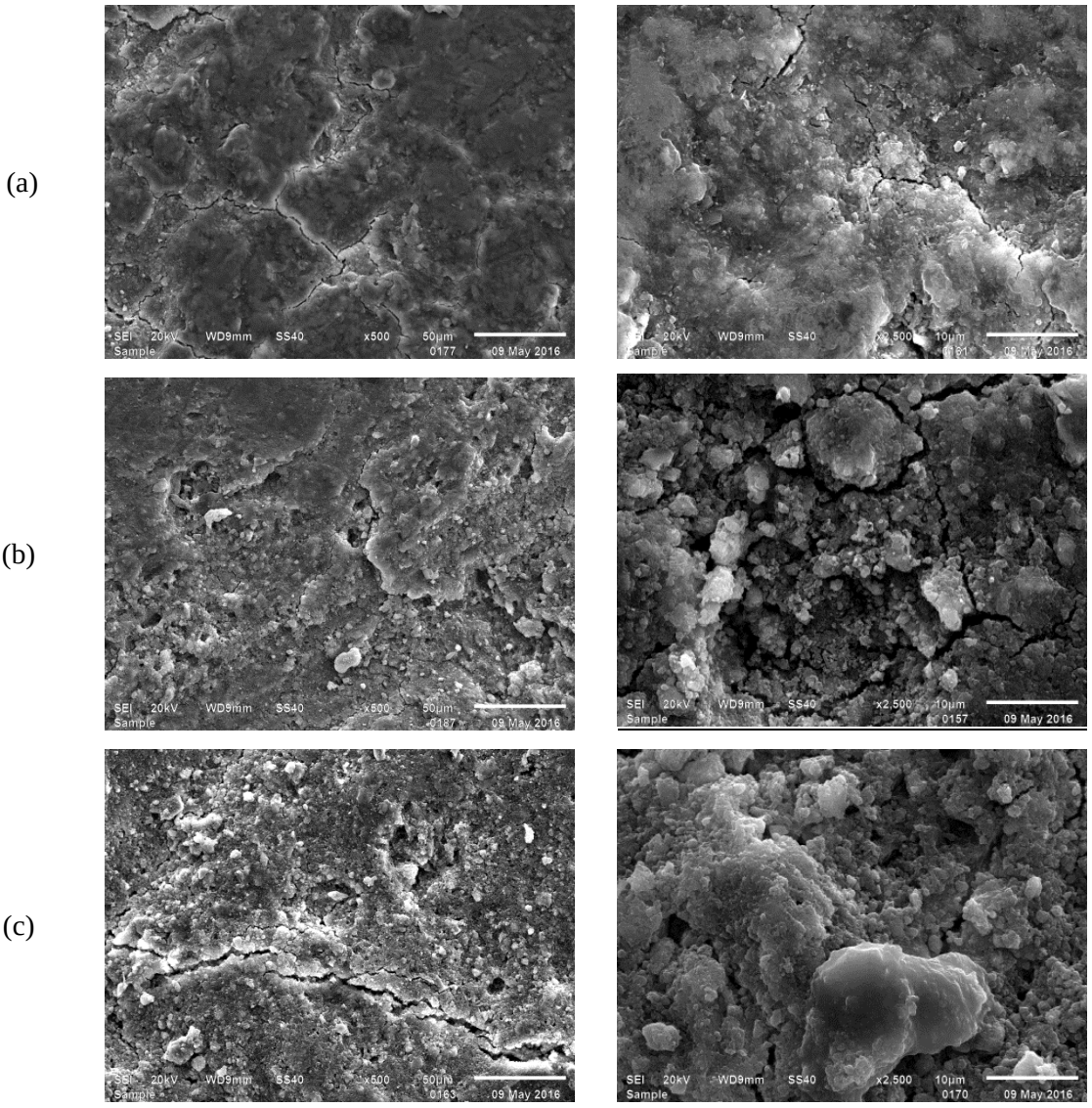

Figure 17. SEI images with 500 (left) and 2500 (right) magnification obtained in: (a) Region V; (b) Region F; and (c) Region N of the trapezoidal plate (w/b = 0.35) at Stage C

5.5 AFM TEST

After the Raman scan and SEM imaging, the samples are polished for the AFM characterization. A grid consisting of 7×7 nodes is mapped on a 30×30 μm region in each sample and then nanoindentation is conducted at each node of the grid. The details of determining the elastic modulus in the AFM nanoindentation can be referred to the work by Tan et al. (Tan, Sherman and Ford, 2004). Based on the modulus obtained at each node, the mechanical properties of matrix microstructure can be quantitatively estimated. In this study, the scanning probe microscopy (SPM) combining multimode V and dimension V is utilized. The surface of the selected representative region is scanned by AFM under contact mode with an NSC15/AIBS silicon probe.

The microstructure topography in Regions V, T and N at Stage C is shown in Figure 18 respectively. Here only the images for the samples of w/b = 0.35 are presented and the similar images for w/b = 0.40 are not shown. The images of Region V clearly show that the C-S-H gels are densely packed and the boundaries between them are clear and smooth in the virgin cement matrix (Figure 18a). While in Figure 18b, the decalcified C-S-H gels in Region T show relatively rough surfaces, which indicate the increase of porosity. Furthermore, the boundaries between C-S-H gels are blurred due to the decalcification. In Region N, the cement matrix, exposed to calcium leaching throughout the entire test, shows a severely degraded microstructure. Due to the chemical attack, the boundaries of C-S-H gels can hardly be distinguished in Figure 18c. In addition, the significant increase of porosity makes the gel surfaces the roughest among the three regions.

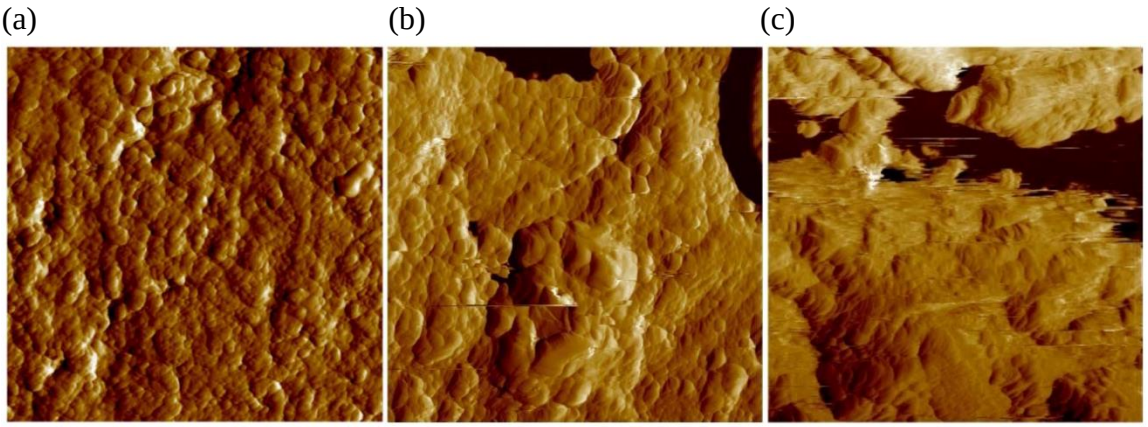

Figure 18. AFM images under contact mode obtained in: (a) Region V; (b) Region T; and (c) Region N of the trapezoidal plate (*w/b* = 0.35) at Stage C

In addition to the topography, the mechanical property of matrix microstructure can be quantitatively characterized based on the modulus distribution. According to the studies by Mondal et al. (Mondal, 2008) and Liu et al. (Liu *et al.*, 2014), the distributions of different phases in cement pastes can be estimated based on the elastic modulus measured at each node of the 7x7 grid. For normal cement pastes, the elastic moduli of the porous phase, C-S-H phase (including both low-density and high-density ones), CH phase and unhydrated cement particles are thought to range from 0 to10 GPa, 10 to 30 GPa, 30 to 60 GPa, and above 60 GPa, respectively (Mondal, 2008). Using these metrics in peak analysis, one can decompose the overall probability distributions of elastic modulus into individual probability distribution of the four constituent phases in cement matrix.

In Figure 19, the overall distribution of modulus (solid line) obtained in Region V is presented for both *w/b* = 0.35 and 0.40. The fitted Gaussian distribution of individual phase (dashed line) is obtained based on peak analysis and further validated by the goodness of fitting based on the Chi-square test. The volume fractions of each phase are estimated based on the individual distribution curve and presented in Table 3. For the virgin matrix, both samples of *w/b*

= 0.35 and 0.40 show that there exist substantial portions of CH and high-density C-S-H phases. For *w/b* = 0.40, the higher content of water leads to more porous and low-density C-S-H phases in the cement matrix.

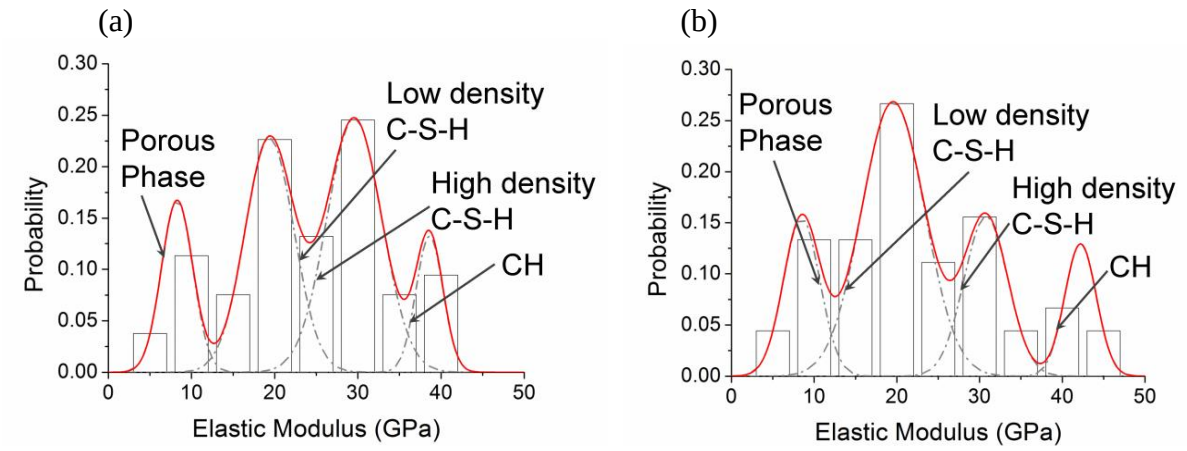

Figure 19. Fitted Gaussian distributions representing virgin cement pastes of: (a) *w/b* = 0.35, and (b) *w/b* = 0.40

Table 3. Moduli and volume fractions of different phases in the virgin cement pastes

	Virgin cement paste (*w/b* = 0.35)		Virgin cement paste (*w/b* = 0.40)	
	E (GPa)	Volume fraction	*E* (GPa)	Volume fraction
Porous phase	8.3 ± 1.89	16%	8.5 ± 2.21	21%
Low-density CSH	19.4 ± 2.94	29%	19.6 ± 3.80	49%
High-density CSH	29.6 ± 3.30	43%	30.1 ± 2.67	17%
CH	38.6 ± 1.63	12%	42.2 ± 1.91	13%

In Figure 20, the overall (solid line) and individual (dashed line) distributions are plotted for *w/b* = 0.35 in Region T. Besides Stage C, the phase distributions at Stages A and B are also

presented here. The calculated volume fraction of each phase at different stages is given in Table 4. It can be seen that the CH phase is entirely leached out even at Stage A. This supports the findings by other researchers, which show that the dissolution of CH phase is much easier than the decalcification of C-S-H gels. The modulus of decalcified C-S-H gels is reduced significantly. Compared with the virgin matrix, the average moduli of decalcified C-S-H gels approaches 10 GPa, the limit to distinguish porous phase and low-density C-S-H gel. In Table 3 (Chapter 9), it shows that from Stage A to C, the volume fraction of porous phase is almost doubled; while that of C-S-H phase drops by about 80%.

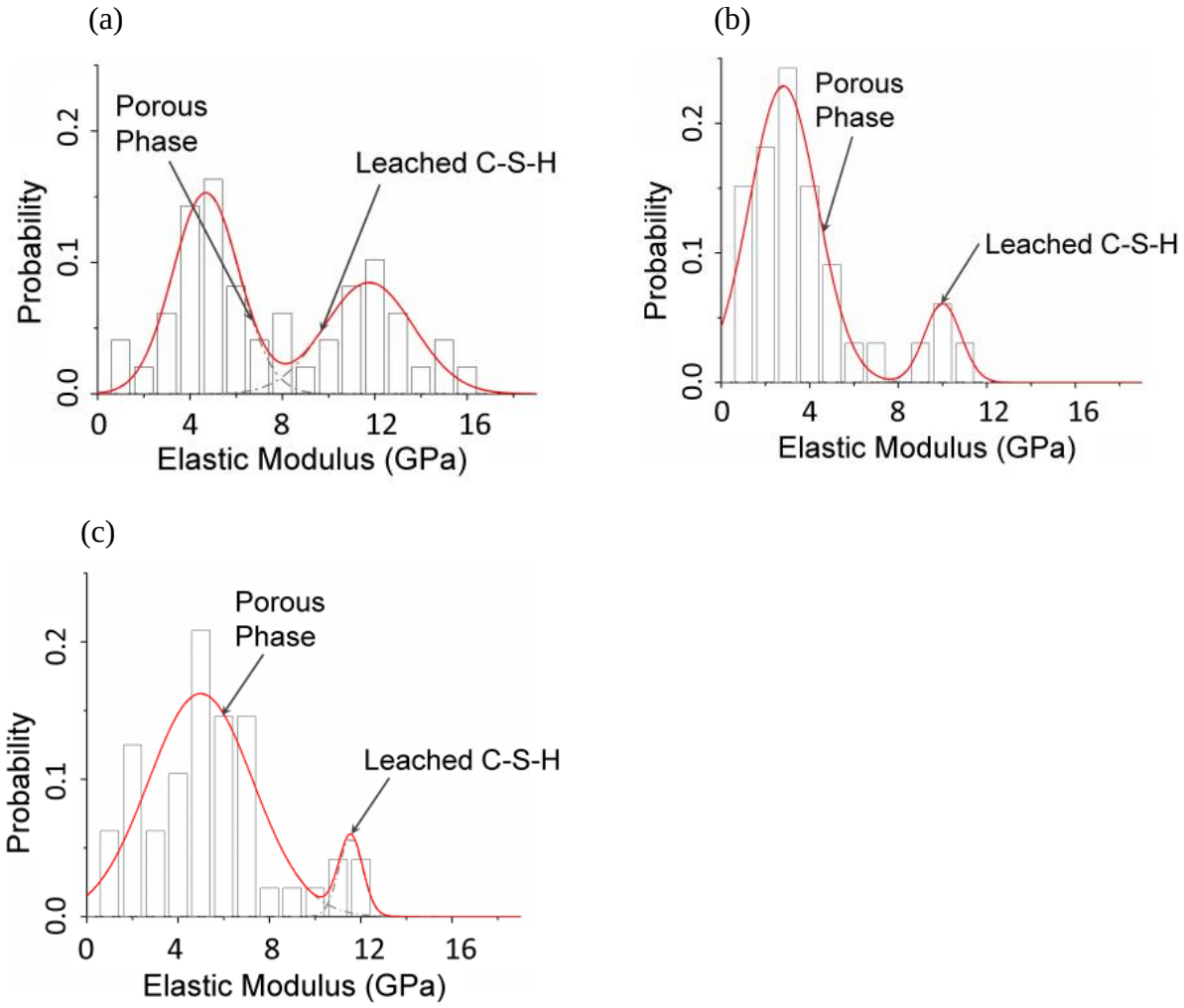

Figure 20. Fitted Gaussian distributions representing cement paste (*w/b* = 0.35) in Region T at: (a) Stage A; (b) Stage B; and (c) Stage C

Table 4. Moduli and volume fractions of different phases in Region T (w/b = 0.35) at different stages

	Stage A		Stage B		Stage C	
	E (GPa)	Volume fraction	*E* (GPa)	Volume fraction	*E* (GPa)	Volume fraction
Porous phase	4.52 ± 1.42	57%	2.80 ± 1.50	87%	4.90 ± 2.30	92%
CSH phase	11.74 ± 1.93	43%	10.0 ± 0.82	13%	11.5 ± 0.5	8%

One thing needs to be mentioned here is that although the AFM nanoindentation is conducted on a grid consisting 49 nodes, it only covers a small region of the matrix microstructure. Thus, this quantitative characterization is only effective for this location. Considering the material randomness of cement pastes, it is more appropriate to use this local quantification to qualitatively evaluate the overall mechanical property of cement matrix.

6.0 MODELING OF COUPLED CHEMO-MECHANICAL DETERIORATION

As documented in the micro- and macro-characterization, the material constants and chemical compositions of the constituents in cement matrix vary substantially during the process of chemo-mechanical deterioration. According to the theory of mixtures (Wan, Li and Sun, 2013), a key physical variable interlinking these changes is the interconnected pores in the cement matrix. Dictated by the laws of chemical equilibrium and mass conservation, the solid phases in the material skeleton are dissolved and then transported in the pore fluid. As a result of dissolution, the pore space increases and the material skeleton is weakened. Under the external loads, subcritical cracks grow and coalesce in some weakened members of skeleton, which improves the transport of reaction products, and thus further accelerates the dissolution of cement matrix.

Based on Kuhl et al. (Potyondy, 2007), the volume fraction of total pore space ϕ in the cement matrix can be decomposed into three parts as follows:

$$\phi = \phi_0 + \phi_c + \phi_m \tag{7}$$

where ϕ_0 represents the initial porosity of intact matrix; ϕ_c is the porosity growth resulting from calcium leaching; and ϕ_m accounts for the fracture-induced microcracks in the material skeleton. Note that neither ϕ nor ϕ_0 includes the nano-pores ϕ_n in the hydration gels (i.e., material skeleton). This is due to the fact that the transport of aggressive ions into these extremely small

pores is difficult. Since there is no mass transport and phase change involved in skeleton fracture, the microcrack-induced porosity ϕ_m is deemed only related to the transport and mechanical properties of material skeleton, but not to the chemical equilibrium and matrix dissolution. In other words, the chemical reaction of calcium leaching is only related to the ion concentration in the pore fluid occupying the pore space of ϕ_0 and ϕ_c. In Figure 21, different types of porosity and their roles in mechanical response and mass transport are schematically depicted.

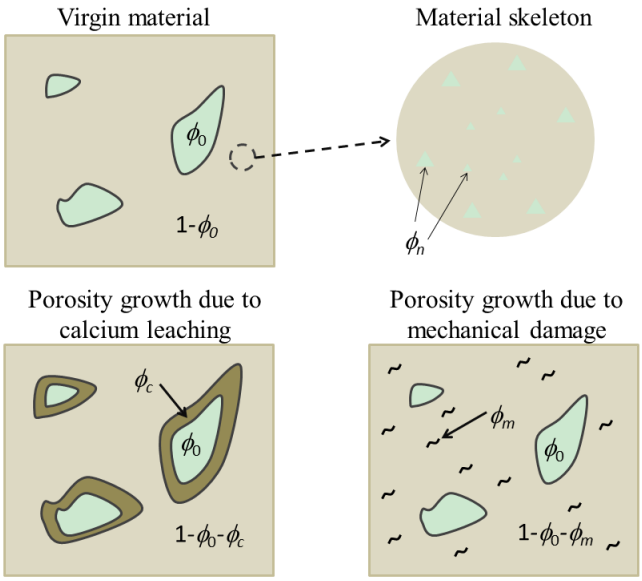

Figure 21. Different types of porosity in the cement matrix

6.1 INITIAL CHEMICAL COMPOSITIONS

Although the chemical equilibrium between the pore solution and the solid constituents of material skeleton is complex, the calcium ion concentration in the pore fluid is generally deemed as a primary variable to describe the state of calcium leaching (Mainguy and Coussy, 2000; Gérard, Le Bellego and Bernard, 2002). Among many contributors of the hydration products,

calcium hydroxide (CH), aluminates (AF) and C-S-H gels are considered the primary sources of calcium ion during the matrix dissolution. Since the content of AF is almost negligible when compared with those of CH and C-S-H gels, it will be ignored in the leaching reaction in this study.

To estimate the initial contents of CH and C-S-H in the cement matrix before leaching, information about the mineral composition of cement clinker and the hydration degrees of compounds is needed. For simplicity, Bogue equation (Fuchs, 1994) is adopted here and only the two main clinker phases C_3S (tricalcium silicate) and C_2S (dicalcium silicate) are considered for ordinary Portland cement. This leads to the following set of stoichiometric reactions in hydration (Wan, Li and Sun, 2013):

$$\begin{aligned} C_3S+5.3H &\rightarrow 0.5C_{3.4}S_2H_8+1.3CH \\ C_2S+4.3H &\rightarrow 0.5C_{3.4}S_2H_8+0.3CH \end{aligned} \tag{8}$$

In addition to the curing time t, the degree of hydration mainly depends on the water-cement ratio and curing conditions. Normally, the rate of hydration can be approximated based on Avrami equation as follows:

$$\xi_i = 1 - e^{-a_i (t-b_i)^{c_i}} \tag{9}$$

where ξ_i are the hydration degrees of compounds at time t (in days), and the subscripts i = 1 and 2 represent C_3S and C_2S respectively. Here the constants a_i, b_i and c_i are determined empirically and their typical values for a specific Portland cement can be found in the work by Tennis and

Jennings (Tennis and Jennings, 2000). The overall hydration degree ξ is then defined based on the mass fractions m_i of C_3S and C_2S as follows:

$$\xi = \sum_i m_i \xi_i / \sum_i m_i \tag{10}$$

During hydration, the volume of cement paste can be assumed to be a constant equal to the simple addition of the volume of cement and water (Gérard, Le Bellego and Bernard, 2002). Thus, the density ρ of the cement paste can be calculated based on the density of cement ρ_c (≈ 3.15 g/cm^3), the density of water ρ_w (≈ 1 g/cm^3) and the water-cement ratio w/b of mix design:

$$\rho = (1 + w/b) / (\frac{1}{\rho_c} + \frac{w/b}{\rho_w}) \tag{11}$$

According to Eqs. 9-11, the initial leachable calcium concentration in pore solutions, expressed respectively in terms of CH (c_{CH}) and C-S-H gels (c_{CSH}), can be calculated as (Wan, Li and Sun, 2013):

$$\begin{aligned} c_{CSH} &= \frac{(1.7\frac{f_{C_3S}}{228} + 1.7\frac{f_{C_2S}}{172})}{\frac{(1+w/b)}{\rho}} \times \xi \times 10^6 \text{(mmol/L)} \\ c_{CH} &= \frac{(1.3\frac{f_{C_3S}}{228} + 0.3\frac{f_{C_2S}}{172})}{\frac{(1+w/b)}{\rho}} \times \xi \times 10^6 \text{(mmol/L)} \end{aligned} \tag{12}$$

where f_{C_3S} and f_{C_2S} are the initial volume fractions of C_3S and C_2S in the cement paste, which can be determined based on the stoichiometric reactions described in Eq. 8.

6.2 CHEMICAL EQUILIBRIUM AND MASS TRANSPORT

During calcium leaching, the chemical equilibrium must satisfy the thermodynamic equilibrium laws. To simplify the chemical analysis, the following assumptions and approximations are made in this study:

1. The re-hydration and leaching of unhydrated cement particles are not considered;
2. At any spatial point, the decalcification of C-S-H gels happens after CH is entirely dissolved;
3. Room temperature is assumed to be constant;
4. The pore fluid pressure is ignored and only the ion diffusion is considered in the mass transport;
5. The time to dissolve a given phase is much shorter than the transport of ions.

Based on these assumptions and approximations, the solid-liquid equilibrium curve, which relates the calcium content *s* in the solid skeleton with the calcium ion concentration *c* in the pore solution, can be employed to describe the thermodynamic equilibrium state of leaching.

The solid-liquid equilibrium curve of calcium has been experimentally determined by quantifying the solubility of cement hydration products in water (Greenberg, Chang and Anderson, 1960), and then applied to calcium leaching models (Gérard, Le Bellego and Bernard, 2002; Wan, Li and Sun, 2013).

In this study, the following solid-liquid equilibrium curve of calcium is used:

$$s(c)=\begin{cases}(-\frac{2}{x_1^3}c^3+\frac{3}{x_1^2}c^2)[c_{CSH}(\frac{c}{c_{satu}})^{1/3}] & 0\le c\le x_1\\ [c_{CSH}(\frac{c}{c_{satu}})^{1/3}] & x_1<c\le x_2\\ [c_{CSH}(\frac{c}{c_{satu}})^{1/3}]+\frac{c_{CH}}{(c_{satu}-x_2)^3}(c-x_2)^3 & x_2<c\le c_{satu}\end{cases} \quad (13)$$

where x_1 is the calcium ion concentration in the pore solution when C-S-H gels are decalcified quickly; x_2 is the concentration when CH is completely dissolved and the decalcification of C-S-H gels begins; c_{satu} is the saturation concentration of calcium ion at room temperature.

For calcium leaching in deionized water at room temperature, the typical values of x_1, x_2 and c_{satu} are 2,(c_{satu} -3), and 20 mmol/L respectively (Gérard, Le Bellego and Bernard, 2002). The corresponding solid-liquid equilibrium curves for cement pastes of different *w*/*b* ratios are plotted in Figure 22a.

However, for ammonium nitrite solutions, in which CH and C-S-H gels show better solubility, the solid-liquid equilibrium curve of calcium has to be modified. For example, it is found that, at room temperature, the saturation concentration of CH will be increased from 20 mmol/L in deionized water to 2730 mmol/L in the ammonium nitrite solution of a concentration = 6000 mmol/L. The values of x_1 and x_2 are supposed to change proportionally to 273 and 2320 mmol/L respectively (Mainguy and Coussy, 2000).

In this study, the concentration of ammonium nitrite solution is 1390 mmol/L. Therefore, the values of x_1, x_2 and c_{satu} are set to be 65, 550 and 650 mmol/L respectively. The solid-liquid equilibrium curves of calcium in this acidic solution for the pastes of different water-cement ratios are shown in Figure 22b.

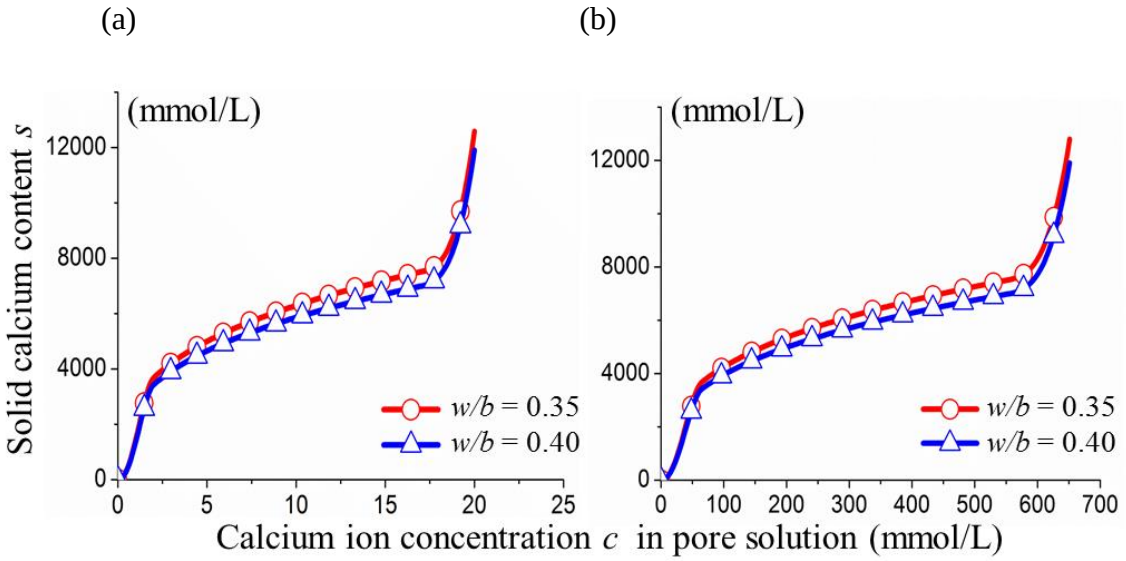

Figure 22. Solid-liquid equilibrium curves of calcium: (a) in deionized water, and (b) in an ammonium nitrite solution of concentration = 1390 mmol/L

To prevent the reverse of matrix dissolution, the chemical reaction criterion proposed by previous studies (Kuhl, Bangert and Meschke, 2004; Potyondy, 2007) is employed here to couple with the solid-liquid equilibrium curve to ensure the thermodynamic equilibrium state. Note that this criterion does not play a major role in this study because the specimens are immersed in an ammonium nitrite solution, whose concentration is maintained during the whole test.

In addition to chemical equilibrium, the calcium ion concentration c in the pore fluid must follow the requirement of mass conservation during leaching. The molar form of the mass balance of calcium ion in the fluid-filled pore space consists of three terms: the spatial change of the mass flux $div\, q$, the rate of mass $\frac{\partial}{\partial t}[(\phi_0 + \phi_c)c]$ due to the temporal variation of the pore space and the calcium concentration, and the dissolution rate of cementitious skeleton $\dot{s}$ (Potyondy, 2007). To satisfy the requirement of mass conservation, the differential equation can be expressed as:

$$div\, q + \frac{\partial}{\partial t}[(\phi_0 + \phi_c)c] + \dot{s} = 0 \tag{14}$$

The mass flux q is determined by the negative concentration gradient of calcium ion:

$$q = D \cdot (-\nabla c) = \phi D_0 \cdot (-\nabla c) \tag{15}$$

where D_0 is the conductivity tensor of pore fluid, which is related to the ion concentration and can be described based on Kohlrausch's law for strong electrolytes (Fuchs, 1994), and D is the macroscopic conductivity tensor, representing the current transport property of cement matrix. Dependence of D_0 on the square root of the calcium concentration within pore fluid is considered. The decrease of conductivity with the increase of calcium concentration can be described as:

$$D_0 = D_{00} - D_{0c}\sqrt{c} \tag{16}$$

6.3 CHEMO-MECHANICAL COUPLING BASED ON POROSITY

During leaching, the porosity growth can be expressed based on the loss of calcium in the material skeleton:

$$\phi_c(c) = \frac{M}{\rho}[s_0 - s(c)] \tag{17}$$

where M/ρ is the average molar volume of CH and CSH gels, s_0 is the initial calcium concentration in the skeleton and $s(c)$ is the current concentration determined by Eq. 13. For the fracture-induced porosity ϕ_m, it can be described based on the damage degree of material skeleton. If a damage scalar parameter d_m is used to describe the growth of micro-cracks, the volume fraction of skeleton can be used to calculate ϕ_m as follows:

$$\phi_m = [1 - \phi_0 - \phi_c(c)]d_m \tag{18}$$

Since ϕ_c is related to dissolution and d_m accounts for skeleton cracking, the mechanical damage and calcium leaching are coupled in Eq. 18. If the SCG happens in the material skeleton, the total porosity ϕ increases with ϕ_m. Thus, the macroscopic conductivity D of matrix grows, which accelerates the ion migration. On the other hand, under calcium leaching, the total porosity ϕ increases with ϕ_c. This weakens the material skeleton and facilitates the growth of subcritical cracks.

6.4 DAMAGE EVOLUTION IN MATERIAL SKELETON

In the context of damage mechanics, the average micro-level stress $\bar{\sigma}$ acting on the undamaged material skeleton is different from the macroscopic nominal stress σ calculated based on the nominal cross section of a specimen body containing many micro- and meso-cracks. Since the skeleton and damaged body can be connected by the total porosity ϕ, it is rational to write the damage law as follows (Voyiadjis, 2012):

$$\sigma = (1-\phi)\bar{\sigma} = (1-\phi)E'\varepsilon \tag{19}$$

where E' is the effective modulus and ε is the effective strain of material skeleton. Under external loads, the damage will accumulate and fracture will happen in the material skeleton. The skeleton cracking can be described by a damage scalar d_m and correspondingly the nominal stress is expressed as:

$$\sigma = (1-\phi_0-\phi_c)(1-d_m)E'\varepsilon \tag{20}$$

To incorporate the kinetics of SCG into the damage law of Eq. 13, the following assumptions are made in this study to formulate the damage rate:

1. Only tensile stress will lead to SCG and fracture, while compressive stress will not;
2. The kinetics of crack growth is proportionally related to the temporal rate of damage scalar d_m;
3. The damage scalar d_m is only dependent on the effective stress $\bar{\sigma}$ in the skeleton.

According to linear elastic fracture mechanics (LEFM), a plane crack will propagate in an elastic medium with a velocity approaching the sound speed once the stress intensity factor K exceeds the critical value K_C at the crack tip (Berner, 1988). Since K at the crack tip depends on the stress induced by external loads, it is rational to assume that when the effective stress in a 1D mechanical element reaches the tensile strength f_t, the stress intensity factor K of the subcritical cracks in this element approaches K_C. This implies that the 1D element fractures

almost instantaneously when its effective tensile stress exceeds f_t. Thus, the time derivative of damage scalar approaches infinity when the material strength is exceeded.

If the stress intensity factor K is less than K_C, the subcritical cracks will grow in the 1D element at a finite velocity. In Chapter 4, the static fatigue test shows that the kinetics of SCG can be described by a straight *K*-*v* curve in the double-logarithmic scale. Correspondingly, the damage rate $\dot{d}_m$ can be approximated by an exponential or power function of the effective stress $\bar{\sigma}$. In this study, a semi-empirical exponential function is adopted. According to the effective stress in the material skeleton, the damage rate can be expressed as follows:

$$\dot{d}_m = \begin{cases} \infty & \bar{\sigma} \geq f_t \\ \beta_1 (e^{\beta_2 (\bar{\sigma}/f_t)} - 1) & \bar{\sigma} < f_t \end{cases} \tag{21}$$

where β_1 and β_2 are two positive constants dependent on the material property of skeleton. Note that in Eq. 15 the threshold effective stress for damage rate is $\bar{\sigma} = 0$. This means that β_1 should be a small value so as to ensure that the velocity of the crack tip is extremely slow (i.e., $v < 10^{-10}$ m/s) when K is less than K_0.

In this formulation of damage rate, the effect of matrix dissolution is incorporated in Eq. 13 implicitly. Under calcium leaching, the total porosity ϕ increases and the cross section of skeleton diminishes. Thus, the effect stress $\bar{\sigma}$ in the skeleton rises if the external load does not change. This increased $\bar{\sigma}$ will accelerate the subcritical crack growth, as well as the damage development in the material skeleton.

7.0 2D DISCRETE MODEL USING TWO LATTICE SYSTEMS

To study the chemo-mechanical deterioration, a 2D discrete model consisting of two lattice systems is constructed in this study. As shown in Figure 23a, the continuous domain of a trapezoidal plate is discretized by two lattice systems, one comprised of 1D transport elements (solid black lines in Figure 23a) and the other comprised of 1D mechanical elements (black dashed lines in Figure 23a). For each element in the lattice systems, its cross-sectional property represents the mechanical property or transport conductivity of a small area in the domain.

Figure 23b shows an area A_{1324} in the continuous domain. The 1D mechanical element, connecting the nodes 1 and 2 (Figure 23b), is used to account for the mechanical property of the area A_{1324}. For each 1D mechanical element, it will be treated as a truss element (Schorn and Rode, 1989; Leite, Slowik and Mihashi, 2004), for which the longitudinal displacement u_x and vertical displacement u_y are used to describe the nodal degrees of freedom. Similarly, the transport conductivity of A_{1324} is represented by the 1D transport element, which links the nodes 3 and 4 (Figure 23b). For each node of the 1D transport element, its nodal degree of freedom is the calcium ion concentration *c* in the pore space. In Figure 23b, the length of elements 1-2 and 3-4 is *h* and *l* respectively. As proposed by Grassl et al. (Grassl *et al.*, 2015), the cross-sectional area of the mechanical element is determined as $A_{12} = l\delta$, where δ stands for the thickness of area

A_{1324}; and the cross-sectional area of transport element is correspondingly calculated as $A_{34} = 0.5hl$.

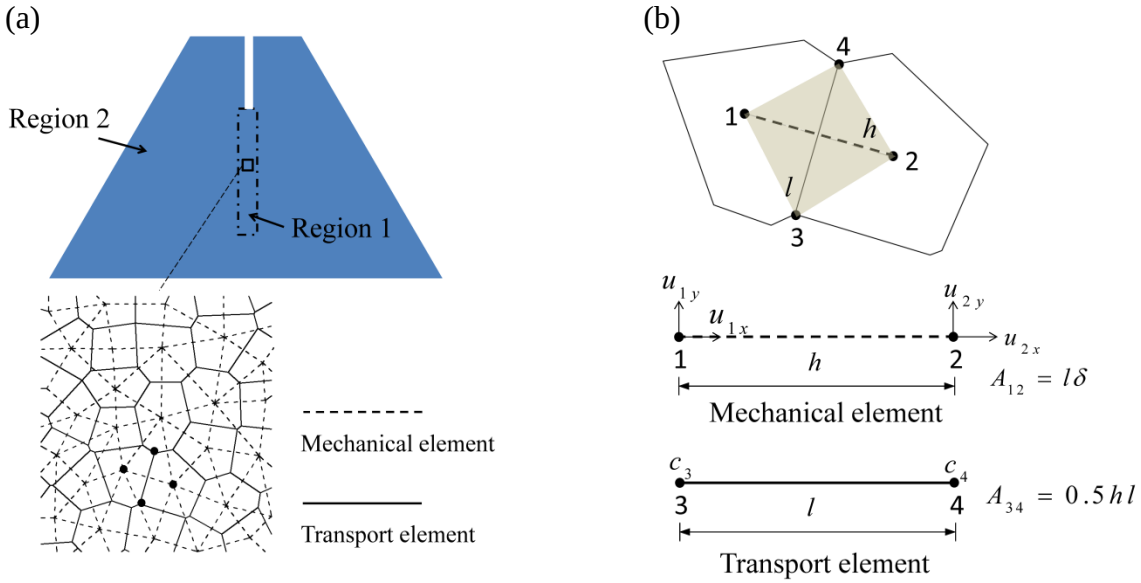

Figure 23. (a) Dual mechanical (dashed line) and transport (solid line) lattices obtained from dual Delaunay and Voronoi tessellation, and (b) nodal degrees of freedom and sectional properties of mechanical and transport elements

If a crack forms in the material skeleton, the ion migration along the crack will be enhanced. To approximate this effect of skeleton cracking on conductivity, the 1D transport element is placed orthogonally to its corresponding 1D mechanical element (Figure 23b) so as to align with the possible crack orientation. To meet this topological requirement, a dual Delaunay and Voronoi tessellation (Aurenhammer, 1991) is employed to generate the mechanical and transport lattice systems. The lattice generation starts with the random placement of seed points within the domain of trapezoidal plate based on a trial-and-error method (Grassl *et al.*, 2015). The seed points are randomly inserted in the domain one by one and a minimum distance $d_{\min}$ is

enforced between two arbitrary seed points. The insertion of seed points stops if after a prescribed number of iterations (e.g., 100,000 iterations) a seed point still cannot be placed in a location that satisfies the minimum distance requirement. At this stage, the domain is considered to be fully saturated by the seed points.

Based on these randomly placed seed points, Delaunay tessellation leads to triangles and Voronoi tessellation results in polygons. The 1D mechanical elements are placed along the edges of Delaunay triangles and the 1D transport elements are along the edges of Voronoi polygons. The length of 1D mechanical elements is implicitly controlled by $d_{\min}$. The smaller $d_{\min}$ is, the shorter is the average length of Delaunay edges. On the other hand, the minimum length of Voronoi edges is not influenced by $d_{\min}$. In Chapters 2-5, the experimental results show that the subcritical crack propagates along the guiding groove where the thickness of plate is $\delta = 3$mm, only half of the other part. Therefore, the plate is divided into two regions based on the groove size (Figure 23a). In Region 1, a fine mesh is used and $d_{\min}$ is set to be 0.4 mm, while in Region 2 the mesh is relatively coarse and $d_{\min}$ is 1.2mm.

Since the seed points are randomly inserted in the domain, they will not be located exactly along the domain boundary. It means the domain boundary cannot be perfectly discretized by the edges of Delaunay triangles or Voronoi polygons. This will lead to some error in the boundary conditions. However, this error is found to be negligible for both mechanical response and mass transport when a fine mesh(which is dictated by $d_{\min}$) is applied (Šavija, Pacheco and Schlangen, 2013). Of course, this error can be entirely eliminated by certain extra operations during the lattice generation, which enforce the edges of triangles or polygons to exactly follow the domain boundary (Grassl *et al.*, 2015).

8.0 NUMERICAL IMPLEMENTATION

In order to couple the numerical analyses performed respectively on the mechanical and transport lattice systems, a hybrid formulation utilizing both implicit and explicit approach is adopted in this study.

Compared to implicit approach, one advantage of explicit approach is that there is no need to assemble the global stiffness matrix and the simulation advances explicitly in time without iteration. Thus, the risk of numerical instability resulting from material softening is mitigated. Therefore, explicit approach is employed to formulate the skeleton cracking in the mechanical lattice system, while for calcium leaching in the transport lattice system, implicit approach is utilized. To take advantage of the pre- and post-processing interfaces provided by general-purpose FEM programs, the material models of this study are programmed in the user-subroutine VUMAT and run under ABAQUS/Explicit solver with the aid of Python script.

8.1 EXPLICIT QUASI-STATIC ANALYSIS

To approximate the kinetics of skeleton cracking, the nonlinear mechanical problem is solved in a quasi-static manner residing on Newton's second law of motion. In a dynamic explicit system, the motion of each node in the mechanical lattice system is described by:

$$M\dot{v} = F^{ext} - F^{\text{int}} \tag{22}$$

where F^{ext} is the external nodal force, F^{int} is the internal nodal reaction, M is the lumped mass at the node and $\dot{v}$ represents the nodal acceleration. Based on the nodal movement, the strain of each truss element can be determined and the corresponding internal nodal reaction can be calculated from Eq. 19.

In explicit analysis, central difference method is generally used to solve Eq. 16 based on the real-time increment Δt. In a dynamic explicit framework, Δt must be less than an upper bound to ensure numerical stability. This upper bound of Δt can be determined by the smallest element size in the mesh and it is usually a small value (e.g., 10^{-5} to 10^{-7} fraction of the total analysis time). This makes the computational analysis of chemo-mechanical deterioration extremely expensive because the deterioration process lasts a long period of time. For example, even when an ammonium nitrite solution of 10% concentration was used to accelerate the stress corrosion test proposed in Chapter 3, it took about 3 months for the subcritical crack to advance over 15 mm.

In order to reduce the computational cost, an artificial time scale, which allows coarse temporal discretization, is employed to replace the real time scale in the explicit quasi-static analysis (Ftima, Sadouki and Brühwiler, 2016). Instead of the real-time increment Δt, a scaled artificial time increment $\Delta \tau$ is used to solve Eq. 16 in the numerical analysis. Here $\Delta \tau$ is less than the upper bound of time increment required by numerical stability, but the time scale factor $\zeta = \Delta t / \Delta \tau$ will map the results to a different time scale. For example, if $\zeta = 3600$, the use of artificial time increment $\Delta \tau = 1$ second will lead to the solutions of displacement and stress fields for a real-time increment $\Delta t = 1$ hour.

For a highly dynamic system, such a time scale factor is not appropriate. However, the SCG in cement pastes subject to chemo-mechanical deterioration is a quasi-static process and the inertia force plays a negligible role. This enables the use of artificial time scale in explicit analysis (Ftima, Sadouki and Brühwiler, 2016). To make sure a proper ζ is selected in the explicit quasi-static analysis, the kinetic energy of mechanical lattice system is compared with the internal energy during the simulation. The conservation of energy requires that the sum of kinetic energy and internal energy is equal to the work done by the external forces. Thus, a quasi-static process is achieved if the kinetic energy is less than 5% of the internal energy at any time step.

8.2 INCREMENTAL FORMULATION OF MASS TRANSPORT

For the 1D transport elements in the lattice system, the rules of mass transport described in Eqs. 8 and 9 can be simplified into a 1D constitutive equation as follows:

$$\frac{\partial}{\partial x}[-\phi D_0 \frac{\partial c}{\partial x}]+[(\phi_0+\phi_c)+c\frac{\partial \phi_c}{\partial s}\frac{\partial s}{\partial c}+\frac{\partial s}{\partial c}]\dot{c}=0$$
$$\dot{\phi}_c=\frac{\partial \phi_c}{\partial s}\frac{\partial s}{\partial c}\dot{c} \quad , \quad \dot{s}=\frac{\partial s}{\partial c}\dot{c} \tag{23}$$

To make it compatible with the governing differential equation used in ABAQUS solver for mass transport, Eq. (14) can be further written as:

$$\frac{\partial}{\partial x}[-\tilde{D}\frac{\partial c}{\partial x}]+\dot{c}=0 \tag{24}$$

where $\tilde{D}$ is the equivalent diffusion coefficient. Based on Eq. 11, $\tilde{D}$ can be expressed as:

$$\tilde{D}=\frac{\phi D_0}{[\phi_0+\phi_c+\frac{\partial s}{\partial c}(1-\frac{M}{\rho}c)]} \tag{25}$$

and

$$\frac{\partial s}{\partial c}=\begin{cases}\frac{1}{3}(-\frac{2}{x_1^3}c^3+\frac{3}{x_1^2}c^2)\frac{c_{CSH}}{(c_{satu})^{1/3}}(c)^{-2/3}+(-\frac{6}{x_1^3}c^2+\frac{6}{x_1^2}c)[c_{CSH}(\frac{c}{c_{satu}})^{1/3}] & 0\le c\le x_1\\ \frac{1}{3}\frac{c_{CSH}}{(c_{satu})^{1/3}}(c)^{-2/3} & x_1<c\le x_2\\ \frac{1}{3}\frac{c_{CSH}}{(c_{satu})^{1/3}}(c)^{-2/3}+\frac{3c_{CH}}{(c_{satu}-x_2)^3}(c-x_2)^2 & x_2<c\le c_{satu}\end{cases} \tag{26}$$

To solve Eq. 18, one may utilize the backward Euler method (modified Crank-Nicholson operator). Different from the mechanical lattice system, the real-time increment Δt can be used here. This is due to the fact that implicit approach is used for formulating the mass transport. Thus, the upper bound of Δt required for numerical stability can be much greater in a mass transport system than that in a dynamic explicit system (Hibbitt, Karlsson and Sorensen, 2011).

8.3 IMPLEMENTATION IN ABAQUS

The coupled chemo-mechanical interaction in the hardened cement pastes is analyzed in ABAQUS based on a staggered scheme. The numerical simulation starts with the mechanical lattice system. During the artificial time increment $\Delta\tau$, the porosity ϕ_c resulting from calcium leaching is assumed to be constant. Subsequently, calcium leaching in the transport lattice system is analyzed in the real time scale. During the real-time increment Δt, it is assumed that the fracture-induced porosity ϕ_m remains unchanged. Then the staggered steps repeat until the total analysis time is reached.

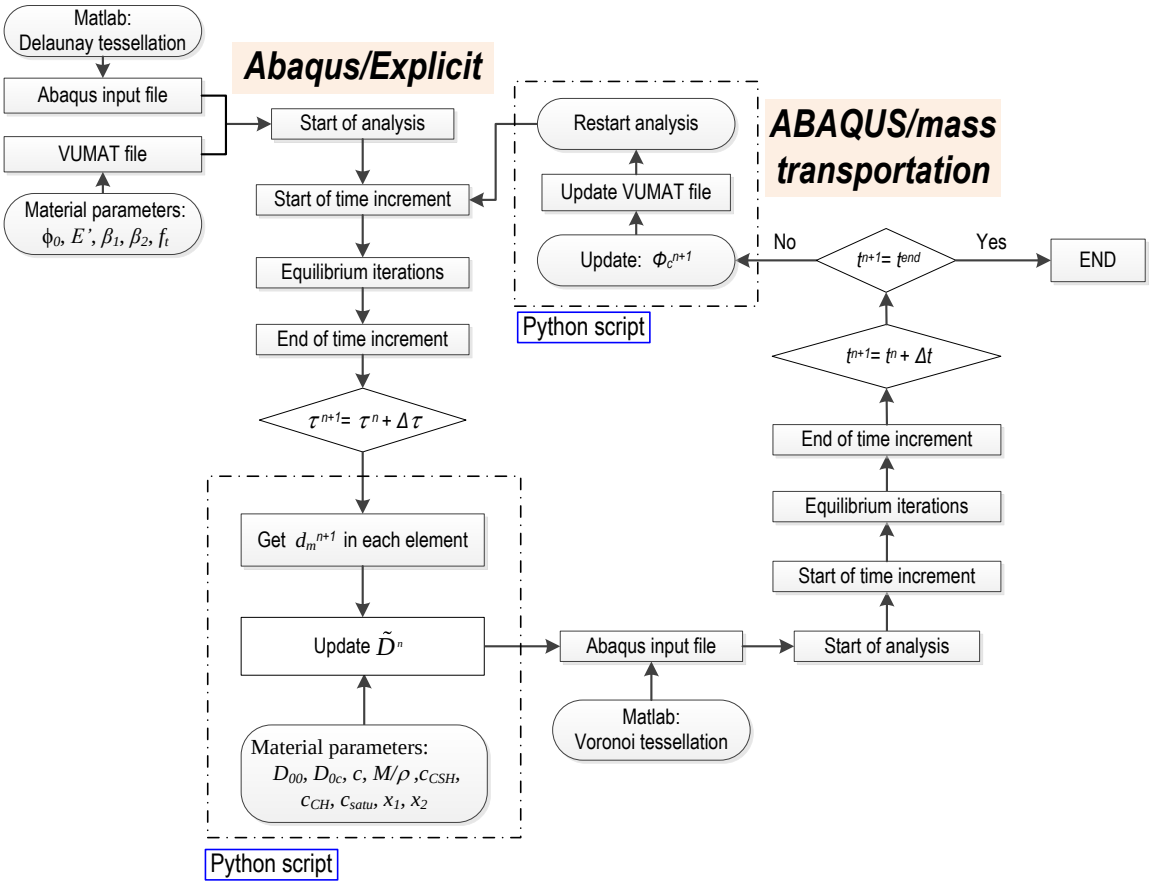

Figure 24. Flow chart of the numerical implementation in ABAQUS

The flowchart of numerical implementation in ABAQUS is given in Figure 24 and a typical staggered process is briefly described here:

1. At the start of time step $\tau^n \rightarrow \tau^{n+1}$ (here the superscript n represents the nth step), the related variables obtained in the last time step, including ϕ_0, ϕ_c^n, ϕ_m^n and c^n, are input into the user subroutine VUMAT;
2. The explicit quasi-static analysis is performed on the mechanical lattice system to obtain the damage scalar d_m^{n+1}, and then ϕ_m^{n+1} is updated at the end of this time step τ^{n+1};
3. The artificial time is scaled to the real time to start the calcium leaching at time step $t^n \rightarrow t^{n+1}$;
4. Based on the damage scalar d_m^{n+1}, the boundary condition of calcium leaching is changed to capture the appearance of cracks;
5. Based on the values of related variables at t^n, the equivalent diffusion coefficient $\tilde{D}^n$ of each transport element is determined;
6. The calcium concentration c^{n+1} in the pore solution and the dissolution-induced porosity ϕ_c^{n+1} are updated, by using the mass transport analysis, at the end of time step t^{n+1};
7. The real time is scaled to τ^{n+1} to start the next staggered process.

In this study, if d_m reaches 1.0, the truss element is deemed to be totally fractured and an apparent crack is generated. Since the plate is immersed in an acid solution, the boundary condition needs to be changed in step 4 to capture the exposed crack surfaces.

In this staggered scheme, two ABAQUS solvers, namely the explicit solver and mass transport solver, will be called sequentially. The transition between the two solvers is automatically achieved by a program coded in the Python script.

9.0 SIMULATION RESULTS AND COMPARISONS

Multiple simulations are run in ABAQUS and the obtained numerical results are compared with the experimental results recorded in Chapter 8. The comparison includes the results of calcium leaching test, static fatigue test and stress corrosion test. For each batch of specimens, the same set of model parameters is used. The parameters used for water-cement ratios w/b = 0.35 and 0.40 are given in Table 5.

Except for D_{00}, D_{0c}, β_1 and β_2, the model parameters are obtained directly from the material tests or estimated through the recommended formulas based on the mix design. The parameters D_{00} and D_{0c}, which are related to the conductivity property of hardened cement pastes, are calibrated based on the calcium leaching test. The parameters β_1 and β_2, which describe the crack-growth rate, are calibrated with the static fatigue test. Based on the ACI empirical formulas, it is found that the aging effect on strength and modulus is negligible. Thus, this aging effect of concrete is not considered in the simulations.

Table 5. Parameters used in the simulations

w/b= 0.35	w/b= 0.40
$E' = 27.4\,\text{GPa}$	$E' = 22.5\,\text{GPa}$
$f_t = 4.2\,\text{MPa}$	$f_t = 4.0\,\text{MPa}$
$\phi_0 = 0.160$	$\phi_0 = 0.210$

Table 5 (continued).	
$C_{CSH} = 7928\ \text{mmol/m}^3$	$C_{CSH} = 7376\ \text{mmol/m}^3$
$C_{CH} = 4651\ \text{mmol/m}^3$	$C_{CH} = 4328\ \text{mmol/m}^3$
$D_{00} = 0.70\times10^{-10}\ \text{m}^2/\text{s}$	$D_{00} = 1.10\times10^{-10}\ \text{m}^2/\text{s}$
$D_{0c} = 1.40\times10^{-12}\ \text{m}^2/\text{s}\sqrt{\text{m}^3/\text{mol}}$	$D_{0c} = 2.20\times10^{-12}\ \text{m}^2/\text{s}\sqrt{\text{m}^3/\text{mol}}$
$\beta_1 = 3.0\times10^{-8}$	$\beta_1 = 4.0\times10^{-8}$
$\beta_2 = 2.5$	$\beta_2 = 3.0$
$c_{satu} = 650\ \text{mmol/L}$ $x_1 = 65\ \text{mmol/L}$ $x_2 = 550\ \text{mmol/L}$ $\frac{M}{\rho} = 3.5\times10^{-5}\ \text{m}^3/\text{mol}$	

9.1 CALCIUM LEACHING TEST

As introduced in Chapter 3, the prismatic specimens are immersed in an ammonium nitrate solution of concentration = 10% to test the development of calcium leaching in the hardened cement pastes. To identify the front of decalcified area after calcium leaching, the phenolphthalein solution is used. For virgin cement paste, the phenolphthalein solution will be pink because the pH value of pore solution is usually over 12.5. While if severe leaching happens, the pH value of pore solution will drop below 9 and correspondingly the phenolphthalein solution will turn to be colorless. Between these two pH values, the color of phenolphthalein solution will show a transition between these two colors.

In the recent studies (Le Bellégo, Gérard and Pijaudier-Cabot, 2001; Nguyen *et al.*, 2007), it is found that the dissolution of CH phase occurs when the pH value of pore solution drops below 12. This means the real leaching front is ahead of the colorless area, where pH value drops below 9 due to the severe dissolution and decalcification. To estimate the actual decalcification depth d_f in hardened cement pastes, an empirical formula (Le Bellégo, Gérard and Pijaudier-Cabot, 2001) is used here

$$d_f = 1.17 d_p \tag{27}$$

where d_p is measured based on the colorless area after the phenolphthalein solution is sprayed.

Results of the calcium leaching test on three prisms, which are made from the same batch of the mix with w/b = 0.35 and immersed in the acid solution for 42, 72, and 89 days respectively, are shown in Figure 25 and compared with the computational results. It can be seen that the development of calcium leaching captured in the simulations agrees well with the test. In Figure 25a, the development of decalcification depth d_f with time is plotted for w/b = 0.35. Here d_p is determined based on the average of six measurements on the cross section of a prism. It also shows the simulated decalcification growth agrees well with the experimental observations. One thing needs to be mentioned is that if the time scale is expressed by the square root of day, both the experiments and simulations show that the decalcification advances in the hardened cement pastes almost linearly with time; see the dashed lines in Figure 25a. This means that the use of diffusion process to describe the calcium leaching in hardened cement pastes is appropriate. Similarly, good agreement is achieved for the specimens of w/b = 0.40, which are shown in Figure 25b.

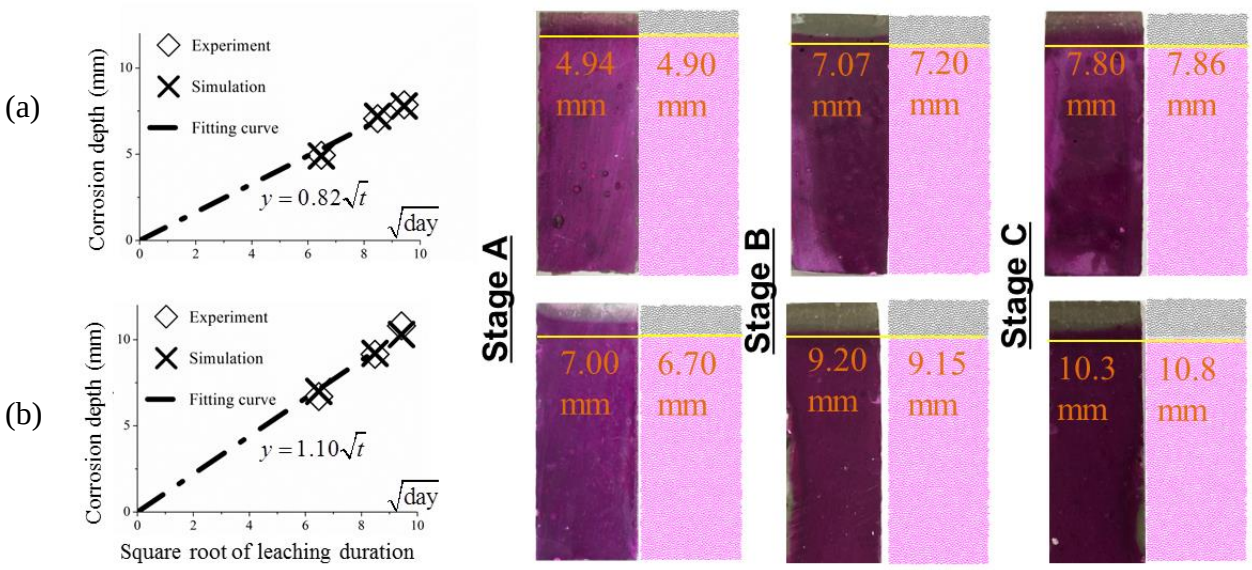

Figure 25. Simulations compared with the prismatic samples subject to calcium leaching: (a) w/b = 0.35, and (b) w/b = 0.40

9.2 STATIC FATIGUE TEST

In Chapter 3, static fatigue test is conducted to probe the subcritical crack growth under constant load. All specimens are immersed in the saturated calcium hydroxide solution to avoid calcium leaching in clean water. The constant load P for the batch of w/b = 0.35 is 35.8N and for w/b = 0.40 is 35.4N.

The crack advance with time recorded in the batch of w/b = 0.35 is plotted in Figure 26a, where the circles, triangles and diamonds represent the measurements on the three plates respectively. It can be seen that the scatter, which is relatively substantial at crack initiation, decreases with the crack propagation. The simulation results, which are represented by the hollow squares, are also plotted in the same figure. It is found that the simulations agree well with the test. Similarly, good agreement is found in the batch of w/b = 0.40; see Figure 26b.

In Figure 27, the *K*-*v* curves measured in the test are plotted for *w*/*b* = 0.35 and 0.40 respectively. When compared with the simulation results (hollow squares), it can be seen that the dependence of crack velocity on the stress intensity factor at crack tip is realistically captured by the numerical model.

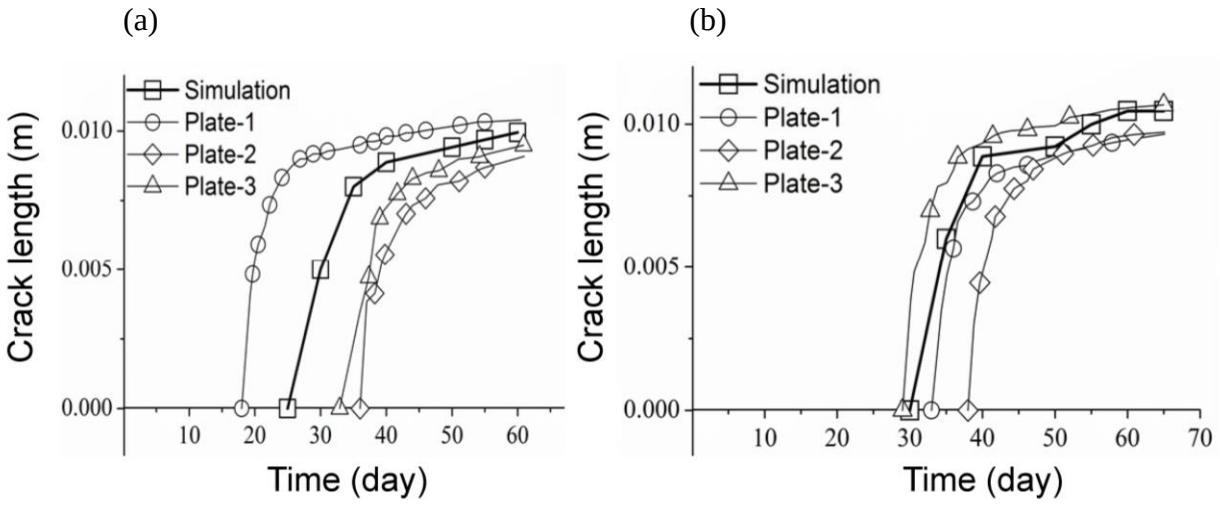

Figure 26. Simulations compared with the crack tip advance in the trapezoidal plates subject to static fatigue: (a) *w*/*b* = 0.35, and (b) *w*/*b* = 0.40

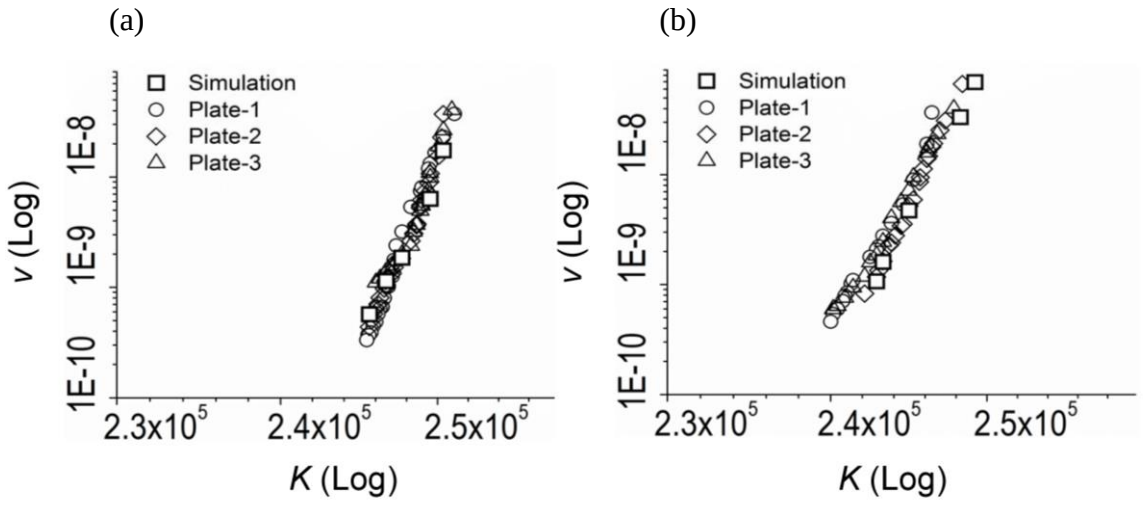

Figure 27. Simulations compared with the *K*-*v* curves of the trapezoidal plates subject to static fatigue: (a) *w*/*b* = 0.35, and (b) *w*/*b* = 0.40

9.3 STRESS CORROSION TEST

For each water-cement ratio, six trapezoidal plates are immersed in the acid solution, among which two specimens are sacrificed during the test. The constant load exerted on the specimens is 26.8N for $w/b = 0.35$ and 26.5N for $w/b = 0.40$.

The crack advance with time recorded in the batch of $w/b = 0.35$ is plotted in Figure 28a, where the two dashed lines represent the specimens sacrificed during the test and the circles, triangles and diamonds document the other four plates respectively. Similar to the static fatigue test, the scatter is relatively great at crack initiation but decreases with the crack propagation. The simulation results, illustrated by the hollow squares, fall within the experimental measurements. This means that the subcritical crack growth subject to stress corrosion is realistically captured in the simulations. Similarly, good agreement is found in the batch of $w/b = 0.40$; see Figure 28b.

In Figure 29, the K-v curves measured in the stress corrosion test are plotted for $w/b = 0.35$ and 0.40 respectively. The K-v curves (hollow squares) obtained in the simulations agree well with the measurements and the three distinctive regions are realistically captured.

In addition to the kinetics of SCG, the development of calcium leach in the trapezoidal plates is compared with the simulation results to further validate the numerical model. The distribution of decalcified area in the specimens, after calcium leaching for 42, 72, and 89 days respectively, is shown in Figure 30. Compared with the experimental results recorded in both

batches (w/b = 0.35 and 0.40), the simulations not only capture the advance of leaching front realistically, but also predict the shape of decalcified area quite well (Figure 30).

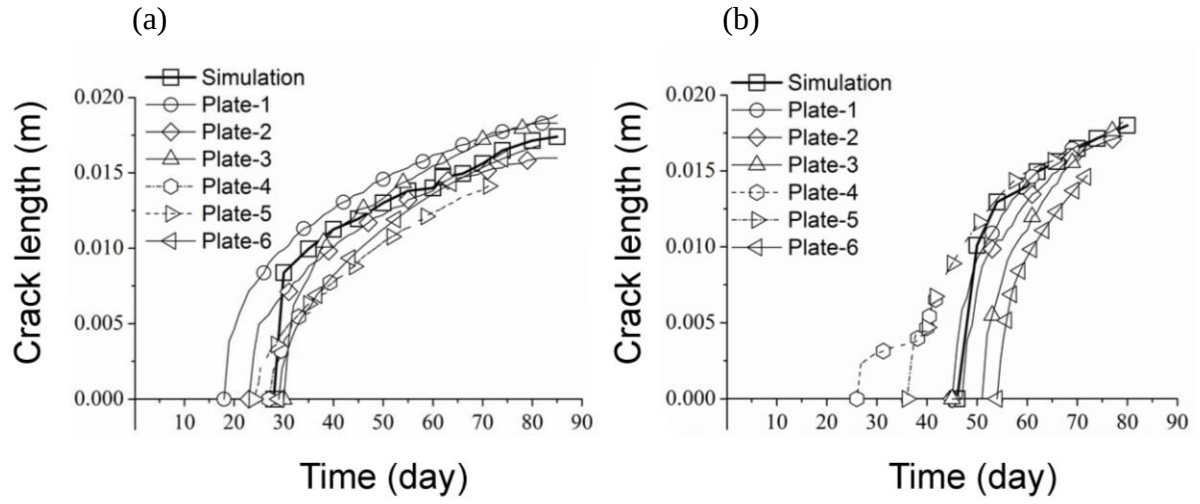

Figure 28. Simulations compared with the crack tip advance in the trapezoidal plates subject to stress corrosion: (a) w/b = 0.35, and (b) w/b = 0.40

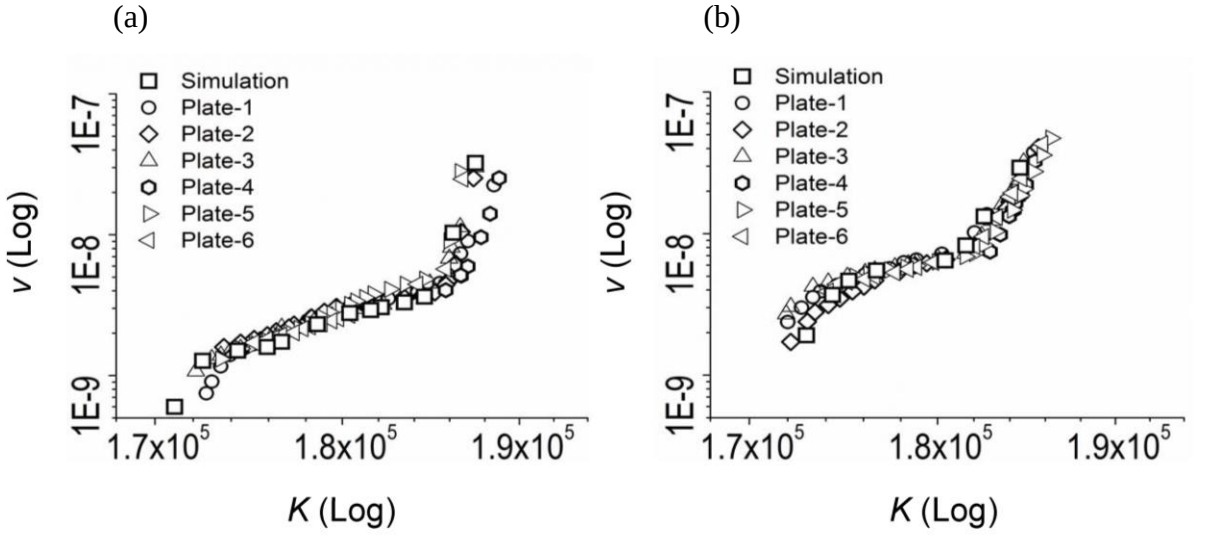

Figure 29. Simulations compared with the K-v curves of the trapezoidal plates subject to stress corrosion: (a) w/b = 0.35, and (b) w/b = 0.40

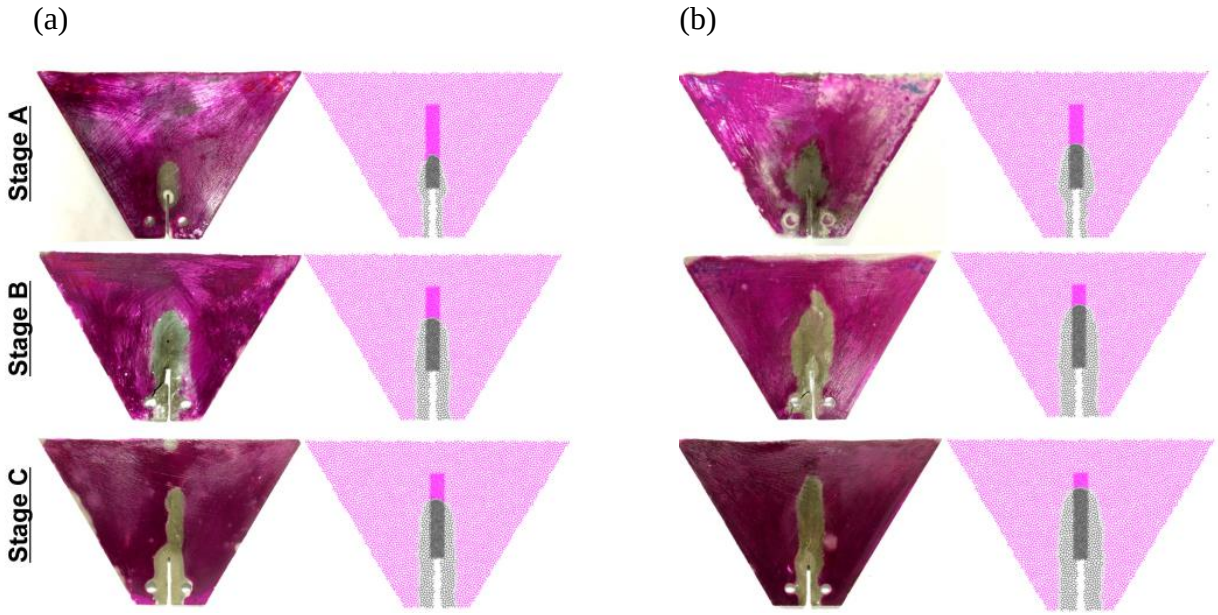

Figure 30. Simulations compared with the decalcified areas in the trapezoidal plates subject to stress corrosion: (a) w/b = 0.35, and (b) w/b = 0.40

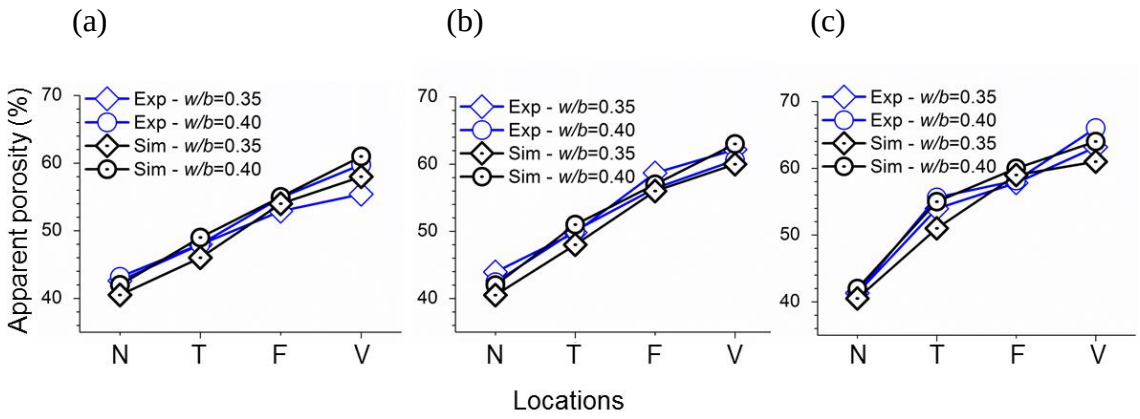

Figure 31. Comparison of apparent porosity: (a) at Stage A; (b) at Stage B; and (c) at Stage C

In Chapter 5.2, the change of apparent porosity during the stress corrosion test is measured. The apparent porosity in Regions N, T, F and V is plotted in Figure 31 for Stage A, B and C respectively, where the circles represent the measurements for w/b = 0.35 and rectangles for w/b = 0.40. For each stage, the average apparent porosity in the corresponding region is also

calculated based on the simulation results. Note that in the numerical model, gel pores of material skeleton are not considered in the total pore space ϕ. Therefore, when compared with the measured apparent porosity, the gel pore space (ϕ_n = 0.36 for *w/b* = 0.35 and 0.41 for *w/b* = 0.40) must be added. Here ϕ_n is estimated based on the AFM test in Chapter 5.5. The predicted apparent porosity, represented by the triangles for *w/b* = 0.35 and diamonds for *w/b* = 0.40, is also plotted in Figure 31. The comparison shows that the numerical model gives realistic estimates of the porosity change for hardened cement pastes subject to stress corrosion.

10.0 CONCLUSIONS

The major goal of the proposed study is to investigate the kinetics of SCG in hardened cement pastes subject to coupled chemo-mechanical attack (particularly, external loading under calcium leaching condition). To attain this goal, a novel experimental method was designed and static fatigue and stress corrosion tests were conducted on specimens of negative geometry. Based on the *K*-*v* curves obtained in both the stress corrosion and static fatigue tests, as well as the results attained in the macro- and micro-characterization, the conclusions drawn from the experimental part of this study include:

1. Specimens of negative geometry are designed to obtain stable subcritical crack growth (SCG) in hardened cement pastes under constant load. With the careful selection of notch length and edge slope, the energy release rate of a trapezoidal thin-plate is found to decrease with the growth of the crack. Thus, specimens of trapezoidal shape are selected and designed for the static fatigue and stress corrosion tests.
2. In order to isolate the influence of coarse aggregates, hardened cement paste is selected as the material of the specimen. Moreover, to accelerate the slow calcium leaching process, ammonium nitrate solution (NH_4NO_3) with 10% concentration is used in the stress corrosion tests.

3. In the stress corrosion test using constant load, three distinctive regions (I, II and III) are found in the obtained *K*-*v* curves in double-logarithmic scale. The slopes of *K*-*v* curves in these regions indicate that the kinetics of SCG is dominated by external force in Region I, governed by mass transport in Region II, and dictated by the chemical-enhanced fracture in Region III. This is very different from the kinetics of SCG in the static fatigue test, in which the *K*-*v* curve is almost a straight line in the double-logarithmic scale.
4. The experimental method presented in this study is capable of testing multiple specimens at the same time. This is important to quantify the average trend and the associated variation of SCG subject to chemo-mechanical deterioration. Furthermore, this makes it possible to sacrifice specimens at the scheduled time intervals to investigate the changes in the macroscopic property and microstructure.
5. The *K*-*v* curves show that if the hardened cement paste is weaker, SCG will start at a lower load. This is documented by the values of threshold stress intensity factor K_0 of w/b = 0.35 and 0.40. If K_0 obtained in the stress corrosion test is compared with that in the static fatigue test, it can be seen that with the aid of calcium leaching, the SCG can happen in the hardened cement pastes at a much lower load.
6. The macro-characterization discovers that the apparent porosity of cement paste increases significantly due to the dissolution and decalcification. This enhances the conductivity of cement pastes. Compared with the process of calcium leaching alone, the superposition of mechanical damage can substantially accelerate the

decalcification of cement pastes. However, this acceleration is not isotropic. Instead, it primarily follows the orientations of cracks.

7. In the micro-characterization, it is observed that the calcium leaching causes chemical changes of the compounds in cement pastes. The spectrum peaks of CH phase found in the virgin matrix by Raman scan disappear quickly after calcium leaching. The SEI contrast images also show the increase of porosity and loss of material skeleton due to the decalcification.
8. The destruction of matrix microstructure is quantified by the AFM test. Based on the elastic moduli measured at the nodes of a grid, the distributions of different phases in the matrix microstructure are estimated. It shows that CH phase is quickly dissolved in calcium leaching. With the development of decalcification, the modulus of C-S-H phase is significantly reduced and the volume fraction of porous phase is substantially increased.

The results obtained in the tests provide not only macro- and microscopic information for deeper understanding of the SCG in cement-based materials, but also important benchmarks for the numerical modeling of chemo-mechanical deterioration.

In the numerical simulation of this thesis, the material models and constitutive laws are constructed to estimate the coupled effect of mechanical damage and calcium leaching on the subcritical crack growth in hardened cement pastes. The hardened cement pastes, which are treated as a porous medium composed of inter-connected fluid-filled pores and cementitious skeleton, is discretized with two lattice systems in the numerical model.

Based on the comparisons between the experimental benchmarks and results of numerical simulations, the following conclusions can be drawn:

9. During calcium leaching, the dissolution of material skeleton is much faster than the diffusion process of ions. Therefore, the solid-liquid equilibrium curve of calcium can be used to describe the thermodynamic equilibrium state of leaching. The simulation results obtained from both batches of prismatic specimens show that the solid-liquid equilibrium curve, which can be determined based on the mix design, gives a realistic prediction of the dissolution front.
10. The SCG in the trapezoidal specimens can be approximated by the damage accumulation in the material skeleton. The damage rate can be expressed by an exponential function based on the effective tensile stress in the material skeleton. The simulation results show that this exponential function gives a good description of the subcritical crack growth in the static fatigue test.
11. The two-way coupling between calcium leaching and mechanical damage can be anchored at the pore space of hardened cement paste. The formulation of the effect of porosity on matrix conductivity, as well as the effect of damage on pore space, leads to a good approximation of the subcritical crack growth subject to stress corrosion.
12. The two lattice systems, which are generated by a dual Delaunay and Voronoi tessellation, not only constitute a discrete model to simulate the chemo-mechanical deterioration, but also provide an effective approach to reproduce the effect of skeleton cracking on matrix conductivity. It is shown that both the crack advance and matrix dissolution are captured well in this discrete model.
13. The SCG in cement pastes is a quasi-static process, which allows the use of artificial time scale in the explicit analysis. This can significantly reduce the

computational cost resulting from the slow process of chemo-mechanical deterioration.

For studies on cementitious materials such as cement paste, mortar and concrete, it is usually considered important to monitor the change in typical mechanical properties, including compressive and tensile strength, Young's modulus, Poisson's ratio and etc., as a function of the long-term deterioration evolution. By monitoring these properties, additional information will be provided to deepen the understanding of SCG subject to stress corrosion. However, since the specimens used in this novel test are thin plates, so it becomes extremely difficult to cut cubic samples or beam samples from these plates to test the mechanical changes. Therefore, in this proposed study, an alternative way is conducted to monitor the porosity change, dissolution development, chemical composition change and modulus evolution in the microstructure based on the macro- and micro-characterization. These results will serve as benchmarks and provide the essential information equivalent to the compressive and tensile strength.

Several aspects of these topics can be investigated in future studies:

1. The monitoring of mechanical properties during time evolution is highly recommended, especially for a long-term deterioration test like the stress corrosion test.
2. In order to make the results from the micro-characterization equivalent, the AFM and SEM scans need to be conducted at multiple locations to obtain the average values of microstructure changes, instead of the local quantification at a single representative region.
3. The results of numerical analysis in my study on SCG in cement paste under calcium leaching shows a good match with the experimental results. However,

there are a variety of difficulties when the behavior of SCG is applied to concrete. Further investigations have to take deeper consideration in experimental studies on different factors, such as the aggregate size, the scale of specimen size (to keep the plain stress condition), the proper water-to-cement ratio, the available access to track crack evolution and etc.

4. In this study, creep is not considered in the SCG in cement paste since nominal crack tip is used in this study, which is not closely related to the creep. However, creep will play a role in the SCG in concrete. Similar to the DT test, its primary role is to cause inelastic deformation, which must be excluded in the calculation of specimen compliance so as to find out the equivalent crack tip. It is recommended for future studies to measure the effect of creep during a long-term deterioration test.

BIBLIOGRAPHY

ASTM, C. (2000) '948: Test Method for Dry and Wet Bulk Density', *Water Absorption, and Apparent Porosity of Thin Sections of Glass-Fiber Reinforced Concrete, The American Society for Testing and Materials, West Conshohocken, PA*.

Atkinson, B. K. (1982) 'Subcritical crack propagation in rocks: theory, experimental results and applications', *Journal of Structural Geology*. Pergamon, 4(1), pp. 41–56. doi: 10.1016/0191-8141(82)90005-0.

Atkinson, B. K. (1984) 'Subcritical Crack Growth in Geological Materials', *Journal of Geophysical Research*, 89(10), pp. 4077–4114. doi: 10.1029/JB089iB06p04077.

Aurenhammer, F. (1991) 'Voronoi Diagrams — A Survey of a Fundamental Data Structure', *ACM Computing Surveys*. ACM, 23(3), pp. 345–405. doi: 10.1145/116873.116880.

Bangert, F., Kuhl, D. and Meschke, G. (2001) 'Finite element simulation of chemo-mechanical damage under cyclic loading conditions', *Fracture mechanics of concrete structures*, 1, pp. 145–152. Available at: http://www.framcos.org/FraMCoS-4/145.pdf.

Bazant, Z. P. and Planas, J. (1998) *Fracture and size effect in concrete and other quasibrittle materials*. CRC press.

Beaudoin, J. J. (1985) 'Effect of humidity on subcritical crack growth in cement paste', *Cement and Concrete Research*. Pergamon, 15(5), pp. 871–878. doi: 10.1016/0008-8846(85)90154-1.

Le Belléego, C., Géerard, B. and Pijaudier-Cabot, G. (2001) 'Life-time experiments on mortar beams submitted to calcium leaching', *Creep, Shrinkage and Durability Mechanics of Cement and Other Quasi-Brittle Materials, Amsterdam, Netherlands*, pp. 493–498.

Le Bellégo, C., Gérard, B. and Pijaudier-Cabot, G. (2001) 'Mechanical analysis of concrete structures submitted to an aggressive water attack.', in *Fourth International Conference on Fracture Mechanics of Concrete and Concrete Structures*, pp. 239–246.

Le Bellégo, C., Pijaudier-Cabot, G., Gérard, B., Dubé, J.-F. and Molez, L. (2003) 'Coupled Mechanical and Chemical Damage in Calcium Leached Cementitious Structures', *Journal of Engineering Mechanics*. American Society of Civil Engineers, 129(3), pp. 333–341. doi: 10.1061/(ASCE)0733-9399(2003)129:3(333).

Berner, U. R. (1988) ‘Modelling the incongruent dissolution of hydrated cement minerals’, *Radiochimica Acta*, 44/45(2), pp. 387–393. doi: 10.1524/ract.1988.4445.2.387.

Berner, U. R. (1992) ‘Evolution of pore water chemistry during degradation of cement in a radioactive waste repository environment’, *Waste Management*. Pergamon, 12(2–3), pp. 201–219. doi: 10.1016/0956-053X(92)90049-O.

Bogue, R. H. and La chimie du ciment Portland, E. (1952) *Eyrolles, Paris, France*.

Bolander, J. E. and Berton, S. (2004) ‘Simulation of shrinkage induced cracking in cement composite overlays’, *Cement and Concrete Composites*, 26(7), pp. 861–871. doi: 10.1016/j.cemconcomp.2003.04.001.

Bowen, R. M. (1976) *Theory of mixtures, Continuum physics*.

Cai, W. (2012) *Subcritical crack growth in hardened cement paste*. Eidgenössische Technische Hochschule ETH Zürich. doi: 10.3929/ETHZ-A-007582328.

Cusatis, G., Mencarelli, A., Pelessone, D. and Baylot, J. (2011) ‘Lattice Discrete Particle Model (LDPM) for failure behavior of concrete. II: Calibration and validation’, *Cement and Concrete Composites*, 33(9), pp. 891–905. doi: 10.1016/j.cemconcomp.2011.02.010.

Cusatis, G., Mencarelli, A., Pelessone, D., Baylot, J. and Mencarelli, A. (2011) ‘Lattice Discrete Particle Model (LDPM) for failure behavior of concrete. II: Calibration and validation’, *Cement and Concrete Composites*, 33(9), pp. 881–890. doi: 10.1016/j.cemconcomp.2011.02.010.

Cusatis, G. and Nakamura, H. (2011) ‘Discrete modeling of concrete materials and structures’, *Cement and Concrete Composites*. Elsevier, 33(9), pp. 865–866. doi: 10.1016/j.cemconcomp.2011.08.011.

Evans, A. G. (1972) ‘A method for evaluating the time-dependent failure characteristics of brittle materials - and its application to polycrystalline alumina’, *Journal of Materials Science*. Kluwer Academic Publishers, 7(10), pp. 1137–1146. doi: 10.1007/BF00550196.

Freiman, S. W. (1984) ‘Effects of chemical environments on slow crack growth in glasses and ceramics’, *Journal of Geophysical Research: Solid Earth*, 89(B6), pp. 4072–4076. doi: 10.1029/JB089iB06p04072.

Freiman, S. W., Mulville, D. R. and Mast, P. W. (1973) ‘Crack propagation studies in brittle materials’, *Journal of Materials Science*. Kluwer Academic Publishers, 8(11), pp. 1527–1533. doi: 10.1007/BF00754886.

Ftima, B., Sadouki, H. and Brühwiler, E. (2016) ‘Development of a computational multi-physical framework for the use of nonlinear explicit approach in the assessment of concrete structures affected by alkali-aggregate reaction’, in. doi: 10.21012/FC9.221.

Fuchs, M. (1994) 'The Kohlrausch law as a limit solution to mode coupling equations', *Journal of Non-Crystalline Solids*. North-Holland, 172–174(PART 1), pp. 241–247. doi: 10.1016/0022-3093(94)90442-1.

Fuller, E. (1979) 'An Evaluation of Double-Torsion Testing—Analysis', in *Fracture Mechanics Applied to Brittle Materials*. 100 Barr Harbor Drive, PO Box C700, West Conshohocken, PA 19428-2959: ASTM International, pp. 3-3–16. doi: 10.1520/STP36621S.

Gérard, B., Le Bellego, C. and Bernard, O. (2002) 'Simplified modelling of calcium leaching of concrete in various environments', *Materials and Structures*. Kluwer Academic Publishers, 35(Decemeber), pp. 632–640. doi: 10.1007/BF02480356.

Gerard, B., Pijaudier-Cabot, G. and Laborderie, C. (1998) 'Coupled diffusion-damage modelling and the implications on failure due to strain localisation', *International Journal of Solids and Structures*. Pergamon, 35(31–32), pp. 4107–4120. doi: 10.1016/S0020-7683(97)00304-1.

Gonzalez, A. C. and Pantano, C. G. (1990) 'A Compression-Loaded Double Cantilever Beam Specimen', *Journal of the American Ceramic Society*. Blackwell Publishing Ltd, 73(8), pp. 2534–2535. doi: 10.1111/j.1151-2916.1990.tb07629.x.

Grassl, P. (2009) 'A lattice approach to model flow in cracked concrete', *Cement and Concrete Composites*, 31(7), pp. 454–460. doi: 10.1016/j.cemconcomp.2009.05.001.

Grassl, P., Fahy, C., Gallipoli, D. and Wheeler, S. J. (2015) 'On a 2D hydro-mechanical lattice approach for modelling hydraulic fracture', *Journal of the Mechanics and Physics of Solids*, 75, pp. 104–118. doi: 10.1016/j.jmps.2014.11.011.

Greenberg, S. A., Chang, T. N. and Anderson, E. (1960) 'Investigation of Colloidal Hydrated Calcium Silicates. I. Solubility Products', *The Journal of Physical Chemistry*. American Chemical Society, 64(9), pp. 1151–1157. doi: 10.1021/j100838a012.

Hazle, M. a., Mehicic, M., Gardiner, D. J. and Graves, P. R. (1990) *Practical Raman Spectroscopy*. 1st edn, *Vibrational Spectroscopy*. 1st edn. Edited by D. J. Gardiner and P. R. Graves. Berlin, Heidelberg: Springer Berlin Heidelberg. doi: 10.1016/0924-2031(90)80015-V.

He, M. Y., Turner, M. R. and Evans, A. G. (1995) 'Analysis of the double cleavage drilled compression specimen for interface fracture energy measurements over a range of mode mixities', *Acta Metallurgica Et Materialia*. Pergamon, 43(9), pp. 3453–3458. doi: 10.1016/0956-7151(95)00036-U.

Hibbitt, Karlsson and Sorensen (2011) *ABAQUS: Theory Manual*.

Irwin, G. R. (1958) *Fracture Encyclopedia of Physics, 6*. Springer, Berlin.

Janssen, C. (1977) 'Specimen for fracture mechanics studies on glass', *Revue de Physique Appliquée*. Société Française de Physique, 12(5), pp. 803–803. doi: 10.1051/rphysap:01977001205080300.

Kuhl, D., Bangert, F. and Meschke, G. (2004) 'Coupled chemo-mechanical deterioration of cementitious materials. Part I: Modeling', *International Journal of Solids and Structures*, 41(1), pp. 15–40. doi: 10.1016/j.ijsolstr.2003.08.005.

Lawn, B. R. and Wilshaw, T. R. (1975) *Fracture of brittle solids, 204, CUP, Cambridge, UK*.

Leite, J. P. B., Slowik, V. and Mihashi, H. (2004) 'Computer simulation of fracture processes of concrete using mesolevel models of lattice structures', *Cement and Concrete Research*, 34(6), pp. 1025–1033. doi: 10.1016/j.cemconres.2003.11.011.

Liu, F., Sun, Z. and Qi, C. (2014) 'Raman Spectroscopy Study on the Hydration Behaviors of Portland Cement Pastes during Setting', *Journal of Materials in Civil Engineering*. American Society of Civil Engineers, 27(8), p. 4014223. doi: 10.1061/(ASCE)MT.1943-5533.0001189.

Liu, F., Sun, Z. and Qi, C. (2015) 'Raman spectroscopy of the dehydration process of gypsums', *Advances in Cement Research*. Thomas Telford Ltd , 27(8), pp. 434–446. doi: 10.1680/jadcr.14.00086.

Liu, Q., Tong, T., Liu, S., Yang, D. and Yu, Q. (2014) 'Investigation of using hybrid recycled powder from demolished concrete solids and clay bricks as a pozzolanic supplement for cement', *Construction and Building Materials*, 73, pp. 754–763. doi: 10.1016/j.conbuildmat.2014.09.066.

Machovic, V., Kolar, F., Prochazka, P. P., Peskova, S. and Kuklik, P. (2006) 'Raman Sspectroscopy study of interfacial transition zone in cement compostie reinforced by PP/PE and basalt fibres', *Acta Geodyn. Geomater.*, 3(2), pp. 63–67. doi: 10.1016/S0140-6736(06)68290-1.

Mai, Y. W. and Atkins, A. G. (1980) 'Crack Stability in Fracture Toughness Testing', *The Journal of Strain Analysis for Engineering Design*. SAGE Publications, 15(2), pp. 63–74. doi: 10.1243/03093247V152063.

Mainguy, M. and Coussy, O. (2000) 'Propagation Fronts during Calcium Leaching and Chloride Penetration', *Journal of Engineering Mechanics*. American Society of Civil Engineers, 126(3), pp. 250–257. doi: 10.1061/(ASCE)0733-9399(2000)126:3(250).

Mondal, P. (2008) *Nanomechanical properties of cementitious materials*. ProQuest.

Nadeau, J. S., Mindess, S. and Hay, J. M. (1974) 'Slow Crack Growth in Cement Paste', *Journal of the American Ceramic Society*. Blackwell Publishing Ltd, 57(2), pp. 51–54. doi: 10.1111/j.1151-2916.1974.tb10811.x.

Nguyen, V. H., Colina, H., Torrenti, J. M., Boulay, C. and Nedjar, B. (2007) 'Chemo-mechanical coupling behaviour of leached concrete: Part I: Experimental results', *Nuclear Engineering and Design*, 237(20), pp. 2083–2089. doi: 10.1016/j.nucengdes.2007.02.013.

Potgieter-Vermaak, S. S., Potgieter, J. H., Belleil, M., Deweerdt, F. and Van Grieken, R. (2006) 'The application of Raman spectrometry to the investigation of cement: Part II: A micro-Raman study of OPC, slag and fly ash', *Cement and Concrete Research*, 36(4), pp. 663–670. doi: 10.1016/j.cemconres.2005.09.010.

Potgieter-Vermaak, S. S., Potgieter, J. H. and Van Grieken, R. (2006) 'The application of Raman spectrometry to investigate and characterize cement, Part I: A review', *Cement and Concrete Research*, 36(4), pp. 656–662. doi: 10.1016/j.cemconres.2005.09.008.

Potyondy, D. O. (2007) 'Simulating stress corrosion with a bonded-particle model for rock', *International Journal of Rock Mechanics and Mining Sciences*, 44(5), pp. 677–691. doi: 10.1016/j.ijrmms.2006.10.002.

Sadouki, H. and van Mier, J. G. M. (1997) 'Meso-level analysis of moisture flow in cement composites using a lattice-type approach', *Materials and Structures*. Kluwer Academic Publishers, 30(204), pp. 579–587. doi: Doi 10.1007/Bf02486899.

Šavija, B., Pacheco, J. and Schlangen, E. (2013) 'Lattice modeling of chloride diffusion in sound and cracked concrete', *Cement and Concrete Composites*, 42, pp. 30–40. doi: 10.1016/j.cemconcomp.2013.05.003.

Schorn, H. and Rode, U. (1989) '3-D-Modeling of Process Zone in Concrete by Numerical Simulation', in *Fracture of Concrete and Rock*. New York, NY: Springer New York, pp. 220–228. doi: 10.1007/978-1-4612-3578-1_22.

Shyam, A. and Lara-Curzio, E. (2006) 'The double-torsion testing technique for determination of fracture toughness and slow crack growth behavior of materials: A review', *Journal of Materials Science*. Kluwer Academic Publishers, 41(13), pp. 4093–4104. doi: 10.1007/s10853-005-5553-0.

Standard, A. (1997) 'Standard test method for compressive strength of cylindrical concrete specimens', *C39-86*, pp. 20–24.

Swanson, P. L. (1984) 'Subcritical crack growth and other time- and environment-dependent behavior in crustal rocks', *J Geophys Res*, 89(B6), pp. 4137–4152. doi: Doi 10.1029/Jb089ib06p04137.

Tada, H., Paris, P. C. and Irwin, G. R. (2000) *The analysis of cracks handbook, New York: ASME Press*.

Tan, S., Sherman, R. L. and Ford, W. T. (2004) 'Nanoscale compression of polymer microspheres by atomic force microscopy', *Langmuir*. American Chemical Society , 20(17), pp. 7015–7020. doi: 10.1021/la049597c.

Tennis, P. D. and Jennings, H. M. (2000) 'Model for two types of calcium silicate hydrate in the microstructure of Portland cement pastes', *Cement and Concrete Research*, 30(6), pp. 855–863. doi: 10.1016/S0008-8846(00)00257-X.

Voyiadjis, G. Z. (2012) *Advances in damage mechanics: metals and metal matrix composites*. Elsevier.

Wan, K., Li, Y. and Sun, W. (2013) 'Experimental and modelling research of the accelerated calcium leaching of cement paste in ammonium nitrate solution', *Construction and Building Materials*, 40, pp. 832–846. doi: 10.1016/j.conbuildmat.2012.11.066.

Wang, L. and Ueda, T. (2011) 'Mesoscale Modelling of the Chloride Diffusion in Cracks and Cracked Concrete', *Journal of Advanced Concrete Technology*. Japan Concrete Institute, 9(3), pp. 241–249. doi: 10.3151/jact.9.241.

Wang, W., Tong, T., Tan, S. and Yu, Q. (2016) 'Subcritical Crack Growth in Cementitious Materials Subject to Chemo-mechanical Deterioration - Experimental Test Using Specimens of Negative Geometry', *Manuscript*.

Wecharatana, M. and Shah, S. P. (1980) 'Double torsion tests for studying slow crack growth of portland cement mortar', *Cement and Concrete Research*. Pergamon, 10(6), pp. 833–844. doi: 10.1016/0008-8846(80)90011-3.

Wiederhorn, S. M. (1967) 'Influence of Water Vapor on Crack Propagation in Soda-Lime Glass', *Journal of the American Ceramic Society*. Blackwell Publishing Ltd, 50(8), pp. 407–414. doi: 10.1111/j.1151-2916.1967.tb15145.x.

Wiederhorn, S. M. (1968) 'Moisture assisted crack growth in ceramics', *International Journal of Fracture Mechanics*. Kluwer Academic Publishers, 4(2), pp. 171–177. doi: 10.1007/BF00188945.

Wiederhorn, S. M., Freiman, S. W., Fuller, E. R. and Simmons, C. J. (1982) 'Effects of water and other dielectrics on crack growth', *Journal of Materials Science*. Kluwer Academic Publishers, 17(12), pp. 3460–3478. doi: 10.1007/BF00752191.

Williams, D. P. and Evans, A. G. (1973) 'A Simple Method for Studying Slow Crack Growth', *Journal of Testing and Evaluation*, 1(4), pp. 264–270. doi: 10.1520/JTE10015J.

Xu, S. and Zhu, Y. (2009) 'Experimental determination of fracture parameters for crack propagation in hardening cement paste and mortar', *International Journal of Fracture*. Springer Netherlands, 157(1–2), pp. 33–43. doi: 10.1007/s10704-009-9315-x.